Quantitative evaluation of the lunar seismic scattering and comparison between the Earth, Mars, and the Moon

K. Onodera[1,2,3], T. Kawamura[2], S. Tanaka[4], Y. Ishihara[5], and T. Maeda[6]

[1]Earthquake Research Institute, The University of Tokyo, Tokyo, Japan.

[2]Université Paris Cité, Institut de Physique du Globe de Paris, CNRS, Paris, France.

[3]Department of Space and Astronautical Sciences, The Graduate University for Advanced Studies, SOKENDAI, Kanagawa, Japan.

[4]Institute of Space and Astronautical Science, Japan Aerospace Exploration Agency, Kanagawa, Japan.

[5]JAXA Space Exploration Center (JSEC), Japan Aerospace Exploration Agency, Kanagawa, Japan.

[6]Graduate School of Science and Technology, Hirosaki University, Aomori, Japan.

Corresponding author: Keisuke Onodera (onodera@eri.u-tokyo.ac.jp)

Key Points:

- Through full 3D seismic wave propagation simulation, we quantitatively evaluated the lunar seismic scattering properties.
- We found that a 10 km thick scattering layer with 10% velocity fluctuation well-reproduced the Apollo seismic observation.
- Our results show that the upper lunar crust is about ten times more heterogeneous than that of the Earth and Mars.

Abstract

The intense seismic scattering seen in Apollo lunar seismic data is one of the most characteristic features, making the seismic signals much different from those observed on the Earth. The scattering is considered to be attributed to subsurface heterogeneity. While the heterogeneous structure of the Moon reflects the past geological activities and evolution processes from the formation, the detailed description remains an open issue. Here we present a new model of the subsurface heterogeneity within the upper lunar crust derived through a full 3D seismic wave propagation simulation. Our simulation successfully reproduced the Apollo seismic observations, leading to a significant update of the scattering properties of the Moon. The results showed that the scattering intensity of the Moon is about ten times higher than that of the heterogeneous region on the Earth. The quantified scattering parameters could give us a constraint on the surface evolution process on the Moon and enable the comparative study for answering a fundamental question of why the seismological features are different on various planetary bodies.

Plain Language Summary

In the past Apollo missions, several seismometers were installed on the nearside of the Moon and they brought us the first seismic records from an extraterrestrial body. The derived lunar seismic data surprised us because of their extremely long duration (1 – 2 hours) and spindle-shaped form, which were barely observed on Earth. These characteristics different from earthquakes are thought to reflect the subsurface heterogeneity. However, the inhomogeneous structure within the lunar crust is poorly constrained. To improve our knowledge of wave propagation on an extraterrestrial body, this study evaluated the subsurface heterogeneity through 3D seismic wave propagation simulation. After running some simulations under various structure settings, we found that a certain set of parameters well reproduced the Apollo seismic data, resulting in a new heterogenous structure model of the Moon. The evaluated parameters were compared with those measured on the Earth and Mars, and we found that the Moon is more heterogeneous than others by about ten times. This kind of comparison makes it easier to interpret the observed seismic signals on each solid body. Also, it is useful to explain the differences in their surface evolution scenarios. We believe that our results contribute to further extending comparative planetology.

1 Introduction

The intensely scattered seismic waves with a long duration (1 – 2 hours) and ambiguous phase arrivals (e.g., P, S) are one of the characteristics observed in the Apollo lunar seismic data (Latham et al., 1970; Figure 1a). According to the previous studies on Earth, it is considered that this feature is ascribed to the subsurface heterogeneities such as cracks, igneous intrusions, and faults (Sato et al., 2012 and references therein). While the intense scattering is the essence of the lunar seismic signals, its properties are not fully understood.

In general, estimating the planetary interior using seismic waves relies on precise phase identifications (e.g., P, S arrivals). Yet, the extremely high scattering environment on the Moon makes it more challenging to pick up the phases, leading to considerable uncertainty in the resultant structure model (e.g., Garcia et al., 2019). Thus, it can be said that the scattering is an essential characteristic of the lunar seismic waves, whereas it is the most severe obstacle for the investigation of the lunar internal structure. Moreover, the seismic data from Mars also show intensely scattered features (e.g., Lognonné et al., 2020; Menina et al., 2021), implying that seismic scattering is not just a specific problem in lunar seismology but also a common problem in planetary seismology. Therefore, it is valuable to push forward our understanding of this topic for elucidating the nature of seismic wave propagation on extraterrestrial bodies.

In seismology, there are two important parameters to explain seismic energy decay. The first one is termed “scattering attenuation” — energy loss due to heterogeneity or scatterer — and the second is called “intrinsic attenuation” — energy loss due to the absorption by a medium. To retrieve these parameters, radiative transfer theory (e.g., Aki, 1969; Aki and Chouet, 1975; Sato 1977; Wu, 1985) has been used on the Earth and applied to the Moon and Mars (e.g., Dainty et al., 1974; Dainty and Toksöz, 1981; Menina et al., 2021; Karakostas et al., 2021). In this theory, there are three fundamental situations

considered; single scattering (weak scattering), multiple scattering (intense scattering), and diffusion (extremely intense scattering). The single and multiple scattering conditions are widely applied to earthquakes and also marsquakes (e.g., Aki and Chouet, 1975; Menina et al., 2021), where we can confirm the clear P or S arrival onsets in seismic records (Figure 1b). On the other hand, under extremely intense scattering conditions like the Moon, the diffusion model is preferable (e.g., Dainty et al., 1974), where the seismic phases are well scattered and the waveform shows a spindle shape (Figure 1a).

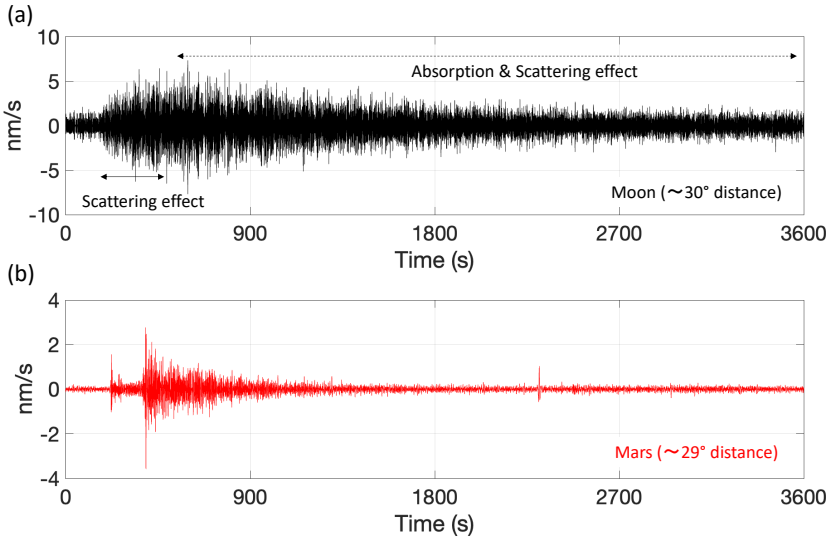

Figure 1. (a) An example of a lunar seismic wave. The horizontal axis shows time in seconds and the vertical shows the velocity in nm/s. This is an impact-induced event recorded on December 15 in 1974 with the vertical component of the long-period seismometer installed at the Apollo 15 landing site. The waveform is bandpass filtered between 0.3 and 1.5 Hz. This event is estimated to have occurred about 30 degrees away from the Apollo 15 station (Oberst, 1989). (b) An example of marsquake (S235b). This event was observed on July 26 in 2019 by InSight (Interior Exploration using Seismic Investigations, Geodesy and Heat Transport) on Mars. The waveform is bandpass filtered between 0.1 and 0.8 Hz. The epicentral distance is about 29 degrees (InSight Mars SEIS data Service, 2019).

For the Moon, the past studies (e.g., Blanchette-Guertin et al., 2012) mainly focused on the energy decay part to evaluate the intrinsic and scattering attenuation. In general, it is challenging to individually assess each contribution, hence the combined effects were obtained. On the other side, the energy growth part (i.e., from the first arrival to the energy peak arrival) reflects forward scattering effects, allowing us to evaluate the scattering attenuation more precisely. In fact, Dainty et al. (1974) tried to model the lunar seismic signals with the diffusion model. While the model well explained the decay part, an energy excess at the energy growth part was observed. This indicates that the diffusion model is not fully capable of explaining the lunar seismic signals, and another approach is required to better understand the scattering effect.

In this study, by employing a more straightforward way than before, we quantitatively evaluate the lunar scattering properties, which have remained an open and severe issue since lunar seismology started. Here, we conduct the first full 3D simulation of seismic wave propagation in this field. The advantage of numerical simulation is that it can consider more complicated problems (or more realistic conditions) while we are forced to assume a simple condition in the analytical modeling. By performing the full 3D simulation, we investigated the lunar scattering effect under the most realistic condition ever considered before. In fact, the 3D simulation costs an extremely large amount of computational resources and limits us to computing only a few hundred of seconds time series. However, our high spatiotemporal resolution simulation enables us to better model the energy growth part, which enables us to evaluate the scattering attenuation effect more precisely than previous approaches.

In the following sections, we present the fundamental idea of the 3D seismic wave propagation simulation and how to compare the simulated results with the observation. Then, we show the results and

discuss the obtained scattering structure within the lunar crust together with the previously proposed models. Finally, we compare our results with the Earth and Mars, and discuss why we observe different seismological features on each solid body. Since this kind of comparative study helps us infer how the evolution processes differ among solid planetary bodies, we believe that our results not just contribute to deepening our understanding of lunar science but also pushing forward comparative planetology.

2 Methodology

In modeling the lunar seismic scattering, we adopted a new approach. The previous works (e.g., Dainty and Toksöz, 1981; Gillet et al., 2017) inverted scattering and attenuation parameters such as scattering attenuation factor (Q_s) and intrinsic attenuation factor (Q_i) based on the radiative transfer theory, where it is considered how incident wave loses the energy due to scattering media and how the shape of energy envelope varies depending on the intensity of heterogeneity (e.g., Sato et al., 2012). Under the intense heterogeneity, this approach works well to explain the decay coda, which strongly reflects the intrinsic attenuation — the energy absorption by medium (e.g., Lognonné et al., 2020). Whereas, the theory is not fully capable of modeling the energy growth part, where the scattering effects are more dominant (Figure 1a). To overcome this problem, we performed forward modeling with 3D seismic wave propagation simulation, including all possible scattering sources such as topographies and wave velocity fluctuation, so to speak, full 3D simulation. The idea is to perform wave propagation simulations under various settings and to find a set of parameters that can well-reproduce the observations. While such an approach was known to be the most straightforward way to evaluate the scattering environment, it was unrealistic to take this approach because it requires a vast amount of computational resources. Recently, accompanied by the significant progress in computational technology, it is now possible to perform the forward approach. In this study, utilizing one of the best supercomputers existing (Earth Simulator 4th generation of Japan Agency for Marine-Earth Science and Technology), we performed the first full 3D simulation in lunar seismology to constrain the scattering properties more directly. In this section, we summarize the key points of the numerical simulation.

2.1 Simulation code for 3D seismic wave propagation

We used the Open-source Seismic Wave Propagation Code (OpenSWPC) developed by Maeda et al. (2017), which is based on the finite difference method with heterogeneity, oceanic layer, and topography (HOT-FDM; Nakamura et al., 2012). The code enables us to include both lunar topographies and scattering media that are mandatory functionalities in this study. Another point is that we realized a stable computation up to 2 Hz, which covers the peak sensitivity frequency band of the Apollo long period (LP) seismometer (0.3 – 1.5 Hz), realizing the first direct comparison between the synthetics and the Apollo data at the same frequency range.

2.2 Reference events and work space

Since this work is the first attempt of full 3D simulation in this field, it is reasonable to start with the artificial impacts because of their well-constrained source locations, origin times, and impact parameters (e.g., kinetic energy, impact angle). Following Onodera et al. (2021) who performed 2D simulation of the lunar seismic wave propagation, we adopted two SIVB rocket booster impacts: Apollo 16 SIVB and Apollo 14 SIVB impacts recorded at Apollo 12 station (Figure 2a). The computational space for each event is shown in Figure 2b-c. The detailed configuration of the simulation is summarized in Text S1 and Table S4.

2.3 Velocity structure

In constructing the velocity model, the gravity data from the Gravity Recovery and Interior Laboratory (GRAIL) mission and the measurements of Apollo returned samples were considered.

Regarding the density structure estimated from the GRAIL data, we used the density and porosity model provided by Besserer et al. (2014). Following their model, the density profile as a function of depth $\rho(z)$ can be written as:

$$\rho(z) = \rho_{surf} + \Delta\rho(1 - e^{-z/d}) \qquad (1)$$

where ρ_{surf} is the surface density, $\Delta\rho$ is the density contrast between fractured surface materials and unfractured bedrock, and d is the e-folding depth. At the Apollo 12 landing region, these parameters take the values of 2,308 kg/m^3, 786 kg/m^3, and 9.8 km, respectively. The porosity as a function of depth $\phi(z)$ can be expressed as:

$$\phi(z) = 1 - \rho(z)/\rho_0 \qquad (2)$$

where $\rho_0 = \rho_{surf} + \Delta\rho$. Substituting Equation 1 into Equation 2 gives us

$$\phi(z) = 1 - \frac{1}{\rho_{surf}+\Delta\rho}\left[\rho_{surf} + \Delta\rho(1 - e^{-\frac{z}{d}})\right]. \qquad (3)$$

In terms of the laboratory measurements, we referred an experimental work by Sondergeld et al. (1979). They constructed an empirical model of the compressional wave velocity $v_p(z)$ based on the measurements of the lunar anorthosite (Apollo sample: #60025, 174) like:

$$v_p(z) = \frac{v_{p0}}{\sqrt{1-\phi(z)}} \exp\left[\frac{(\phi(z)^2-\xi)\phi(z)}{2(1-\phi(z))}\right] \qquad (4)$$

where v_{p0} (= 7.15 km/s) is the P-wave velocity extrapolated from high pressure to zero pressure based on the results by Mizutani and Osako (1974). ξ is an empirical constant and the value ranges from 2 to 24, covering almost all velocity structure models proposed by previous works (Besserer et al., 2014, Sondergeld et al., 1979). In other words, ξ=2 gives the upper limit of the P-wave velocity structure while ξ=24 does the lower limit (Figure 3a). Combining Equation 3 with the empirical velocity structure by Sondergeld et al. (1979) results in the reference model used in the simulations. We employed ξ=7 based on the travel times computed for respective artificial impacts. See Text S2 and S3 for the determination of ξ parameter and additional information about topography and velocity models.

Figure 3a shows the constructed P-wave velocity model. The model consists of three parts: megaregolith (the fragmented structure due to meteoroid impacts), crust, and mantle from top to bottom. It is worth noting that the random media, whose thickness varies from 3.5 to 10 km in the simulation, are inserted in the megaregolith layer. We will explain the scattering layer in the next section. With regards to the V_P/V_S ratio, Lognonné et al. (2003) and Gagnepain-Beyneix et al. (2006) suggested that it could range from 1.7 to 2.0 for high fractured materials. Also, Garcia et al. (2011) employed 2.0 for the top low-velocity layer. In this study, following the previous results, the value in the scattering layer is assumed to be 2.0. Concerning the consolidated layer, $\sqrt{3}$ is given for V_P/V_S. The intrinsic Q used in the simulation was provided combining the results by Nakamura and Koyama (1982) and Blanchette-Guertin et al. (2012) (Table S1).

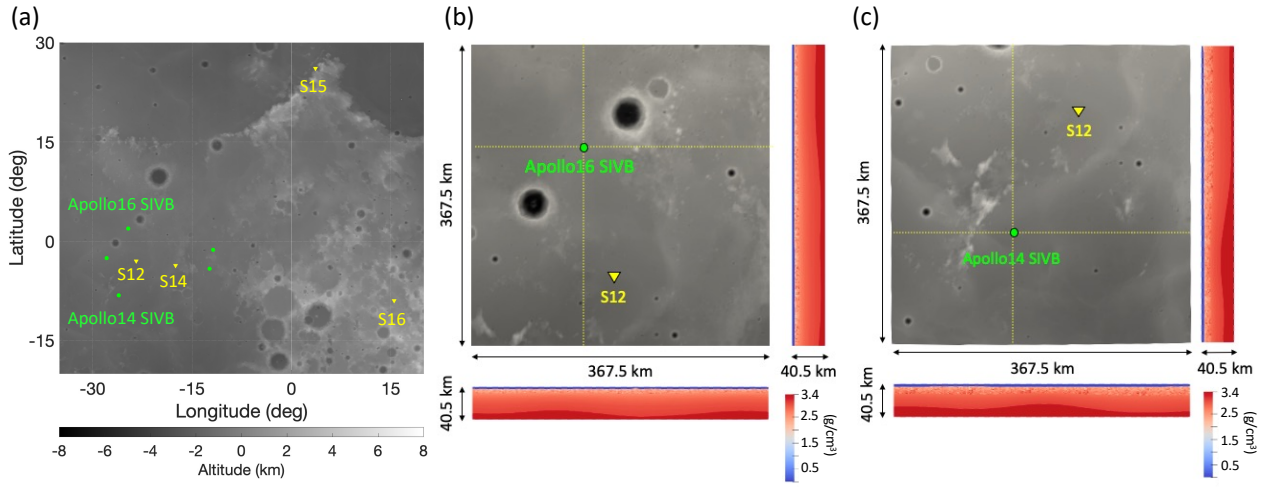

Figure 2. (a) Locations of Apollo SIVB impacts and Stations. The yellow inverse triangles show the locations of the Apollo seismometers and the green circles show the impact locations of the Apollo SIVB rocket boosters. The background is the digital elevation model (DEM) of the SELENE (Kaguya) laser altimeter (Araki et al., 2009). (b) Workspace for the 3D simulation of the Apollo 16 SIVB impact. The bottom and right-hand side panels display the cross-sections of E-W and N-S directions along with the yellow dotted lines. The grayscale corresponds to the surface topography (SLDEM2015; Barker et al., 2016) and the colored scale shows the density within the crust and mantle. The Moho boundary is inserted based on GRAIL crustal model by Wieczorek et al. (2013). Note that the first several km includes random media (i.e., the density fluctuation). (c) Workspace for the 3D simulation of the Apollo 14 SIVB impact. The color scales and each panel are the same as in (b).

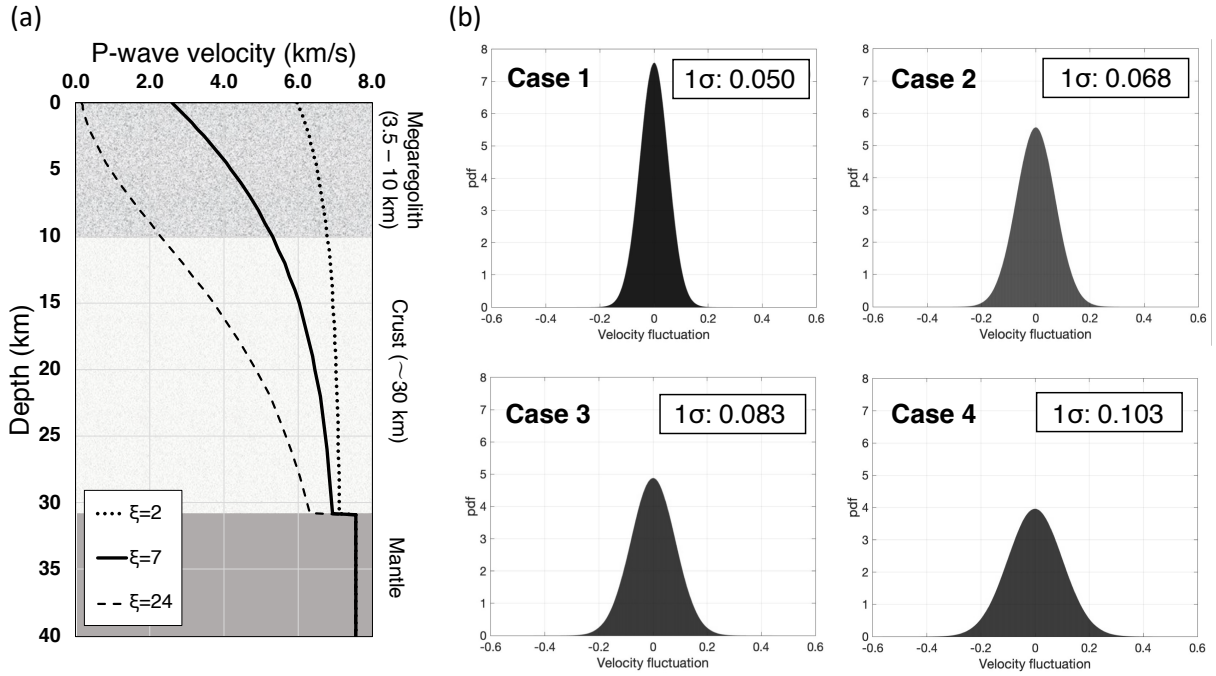

Figure 3. (a) Assumed velocity structure for the simulations. ξ=7 was employed in this work. The structure consists of three parts: megaregolith, crust, and mantle. The random media is inserted into the megaregolith layer. The thickness of the layer varied from 3.5 to 10 km in the simulation. (b) Probability density distribution of the velocity fluctuation of the representative random media used in this study. As the 1σ of the fluctuation gets larger, the scattering effect becomes stronger.

2.4 Scattering model

In terrestrial seismology, the behaviors of seismic scattering have been measured by both laboratory experiments and data analyses of seismic signals (e.g., Sato and Fehler, 1998; Sivaji et al., 2002; Sato et al., 2012). To quantitatively evaluate the properties of seismic scattering due to the heterogeneity inside a medium, previous works investigated the distribution of perturbation from an average velocity and expressed it in a mathematical way using the autocorrelation function (ACF) or power spectral density function (PSDF) (e.g., Shiomi et al., 1997; Sato and Fehler, 1998). According to Sato et al. (2012), there are a few types of ACFs: Gaussian, von Karman, and Exponential. Among these, von Karman or Exponential is usually adopted in the seismological approaches (e.g., Shiomi et al., 1997; Suzuki et al., 1981; Sivaji et al., 2002). We assumed exponential ACF, which is a specific case of von Karman ACF. It is defined as:

$$R(r) = \varepsilon^2 \exp\left(-\frac{r}{a}\right) \qquad (5)$$

where r is lag distance, a is correlation length — the characteristic scale of the heterogeneity within a certain medium, and ε is fractional fluctuation which determines the velocity perturbation from the mean velocity structure.

To simulate the megaregolith (i.e., fragmented rocks by meteoroid impacts), we assumed the isotropic random media, where the correlation length in each direction takes the same value (i.e., $a_X = a_Y = a_Z$), and varied the fractional fluctuation ε from 0.024 to 0.042, corresponding to the 1σ of the velocity fluctuation from 5 to 10%.

Here we focus on the four cases, where the typical scale of random media is fixed to 650 m and 1σ of the velocity fluctuation ranges from 5 to 10% (Figure 3b). The larger perturbation corresponds to more intense scattering (i.e., the scattering effects get stronger from Case 1 to Case 4). The parameter study about the correlation length is presented in Text S4.

Note that these are the parameters for the initial runs to find preferable settings before the further detailed constraints. The additional scattering structure is presented in Section 3.3.

2.5 Source model

As a source model for impacts, there are two approximations; one is the isotropic radiation with moment tensor and the other is the point force (or body force) expressed with the impulse. In past studies, either model was used to simulate the impact-induced seismic waves (e.g., Blanchette-Guertin et al., 2015; Daubar et al., 2020; Onodera et al., 2021). Since the detailed description of the impacts in terms of seismic source modeling is still an open issue, we employed the simplest model — isotropic radiation. In fact, under the intense scattering structure as considered in this study, the radiation information is lost just after the energy is released, and the difference in the source model does not so much affect the resultant waveform (i.e., the structure is much more dominant to characterize the seismogram in this case). Readers can find more details of the source assumption in Text S5.

Besides, in the case of impacts, it is known that there are the shock regime — where plastic deformation occurs — and the elastic regime — where the seismic wave starts to propagate. According to Rajšić et al. (2021), the transition from the shock regime into the elastic regime occurs about 0.15 km away from the Apollo SIVB impact location, which is a much smaller distance than the epicentral distance we consider in this study (> 150 km). Thereby, assuming there is little influence of the shock regime on our results, we pay attention to the elastic regime.

Also, it is worth noting that, through the subsequent simulations, we found that $(1.5 \pm 0.5) \times 10^{12}$ Nm is preferable as the seismic moment, which is equivalent to the seismic energy of $(5.5 \pm 1.8) \times 10^6$ J following Teanby and Wookey (2011). This leads to the seismic efficiency of $(1.2 \pm 0.4) \times 10^{-4}$. Because this is one of the least constrained parameters, we leave a brief note here for future impact physics works.

2.6 Quantitative comparison between synthetics and Apollo data

2.6.1 Preprocessing

First, as generally done in the seismological analysis, a long-term trend is removed from the raw Apollo seismic data. Concerning pre-filtering, the 4-th order Butterworth filter is applied with the cut-off frequency being 0.05 and 3.0 Hz. After that, we applied the Tukey window function with the lobe width being 3% of the data length. Then, the instrumental response of the Apollo LP peaked mode was corrected, which gave us the velocity time series data. After that, we performed the post-bandpass filtering around the peak sensitivity of the LP sensor in peaked mode ($0.3 - 1.5$ Hz).

Because of the radio-tracking of the artificial impacts, the source locations are well-constrained (Table S2 and S3), which enables us to obtain the radial and transverse components using the azimuth information. Note that the seismometer was not aligned in the usual way for Apollo 12, that is, the positive direction of LPX is oriented towards 180°N and that of LPY is towards 270°E.

2.6.2 Estimation of rise-time

As pointed out by Gillet et al. (2017) and Onodera et al. (2021), the energy growth part contains the information of the forward scattering while the decay-coda (i.e., from the peak energy to noise floor) more reflects the diffusion and intrinsic attenuation factors. Since this study focuses on the forward scattering effects, we paid closer attention to the energy growth part. In the following analysis, a parameter called "rise-time"—the time to reach the energy peak from the first arrival—is mainly used. Like P or S arrival reading, the rise-time is determined manually (e.g., Onodera et al., 2021). In the case of the Moon, it is estimated by taking a moving average of the seismic records and detecting the point where the gradient of energy increase becomes flat. In this work, all the seismic signals were smoothed with a window of 200 data points (~30 s). That basically means the uncertainty of the rise-time corresponds to ±15 s.

2.6.3 Equivalent energy density

We looked into the envelope shape in order to track the energy trend in time, which helps us assess how identical the synthetic data are compared to the real one. The seismic energy is proportional to the squared amplitude. Thereby, the equivalent energy E_{eq} is given by:

$$E_{eqi} = \sum {V_i}^2(t) \quad (i = R, T, Z) \qquad (6)$$

where $V(t)$ is the time-series of velocity signal for the radial, transverse, and vertical components. Since this study aims to see how the energy develops with time, we divided the time series into some sections and evaluate the energy density in a certain section instead of computing the total energy. Here, we introduce a new parameter called "equivalent energy density (EED)" E_d defined as:

$$E_{d_j} = \frac{1}{\tau_{j+1} - \tau_j} \sum_{t=\tau_{j+1}}^{\tau_{j+1}} {V_i}^2(t) \quad (i = Z, R, T; j = 1, 2, \dots, 2N_{div} - 1) \qquad (7)$$

$$\tau_n = \frac{nT_{rise}}{N_{div}} \ (n = 1,2, \dots, 2N_{div})$$

where T_{rise} shows the rise-time, and N_{div} (=10 in this study) determines how many sections the time series is divided into. Thereby, the E_d tells us how much energy is received at a station for a certain period, which is useful to track how the energy develops with time.

2.6.4 Amplitude ratio

As another quantitative criterion, we evaluated how much the amplitude at the rise-time A_{rise} differs from the mean amplitude A_{ave}. Figure 4 shows two different cases. The typical lunar seismic signal represents a relatively flat feature after reaching the rise-time, which results in the $A_{\text{rise}}/A_{\text{ave}}$ ratio of ~1.4 (Figure 4a). Note that the time window between the first arrival and $2T_{\text{rise}}$ is used to compute the average value. On the other hand, if a signal has a strong peak as in Figure 4b, the ratio takes a higher value.

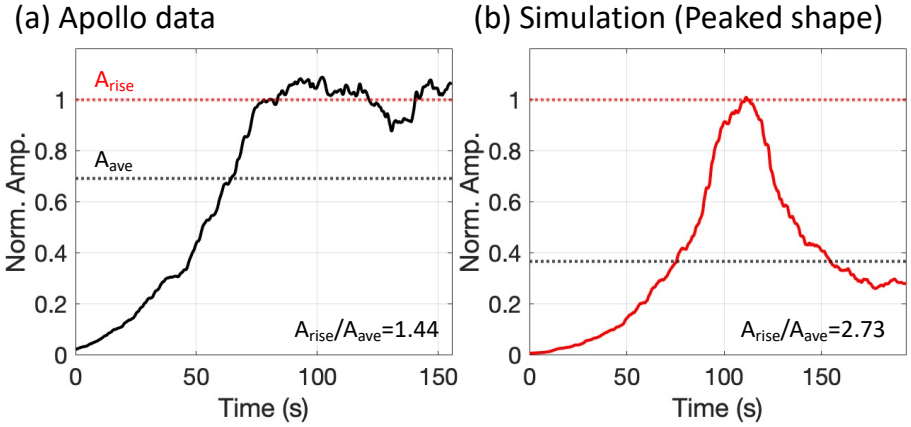

Figure 4. Examples of the amplitude ratio for (a) Apollo data and (b) simulation (Case1). A_{rise} is the amplitude at the rise-time, and A_{ave} stands for the average amplitude between arrival to $2T_{\text{rise}}$.

3 Evaluation of scattering property around the Apollo 12 landing site

As only two events are available in this study, the procedure goes like: (1) constraining the scattering structure for the closer event (Apollo 16 SIVB impact), then (2) applying the structure to another event (Apollo 14 SIVB impact) to see whether the same structure can explain both observations. Unless the structure worked well for two events, a revision in the scattering structure would be given to minimize the discrepancy between synthetics and the data. Section 3.1 shows the results of rise-time, energy trend, and envelope shape for Apollo 16 SIVB impact observed at Station 12. Section 3.2 explains whether the structure based on the Apollo 16 SIVB event also works for Apollo 14 SIVB, and Section 3.3 describes how to improve the scattering structure to better explain both events.

3.1 The initial simulation results for Apollo 16 SIVB impact

Some examples of the simulation outputs are displayed in Figure 5 including snapshots of the horizontal plane (Figure 5a) and the comparison of smoothed energy envelopes for the vertical component between the Apollo (black profile) and synthetics (colored profile) (Figure 5b). Keep in mind that we present the case without scatterer (i.e., only topographies and layered structure are considered) for the comparison in the top row. The snapshots show the time evolution of wave propagation where the red wave shows the compressional component and the green does the shear component. The black circle pattern corresponds to Rayleigh wave (e.g., the second panel in the first row of Figure 5a), which cannot be confirmed in the Apollo data. Thus, one of the important constraints in reproducing the Apollo observation is to attenuate the Rayleigh wave energy to the level of scattered body wave energy. Comparing the four scattering models, it is obvious that the stronger scattering (e.g., Case 4) diffuses the Rayleigh wave energy more rapidly compared to the weaker ones (e.g., Case 1) (Figure 5a). This difference can also be seen in the synthetic waves (Figure 5b). While the synthetic envelope shows a strong peak of the Rayleigh wave in the weak scattering condition (Case 1), as the scattering becomes more intense (Case 4), the Rayleigh wave energy is attenuated and the envelope shape gets more similar to the observation.

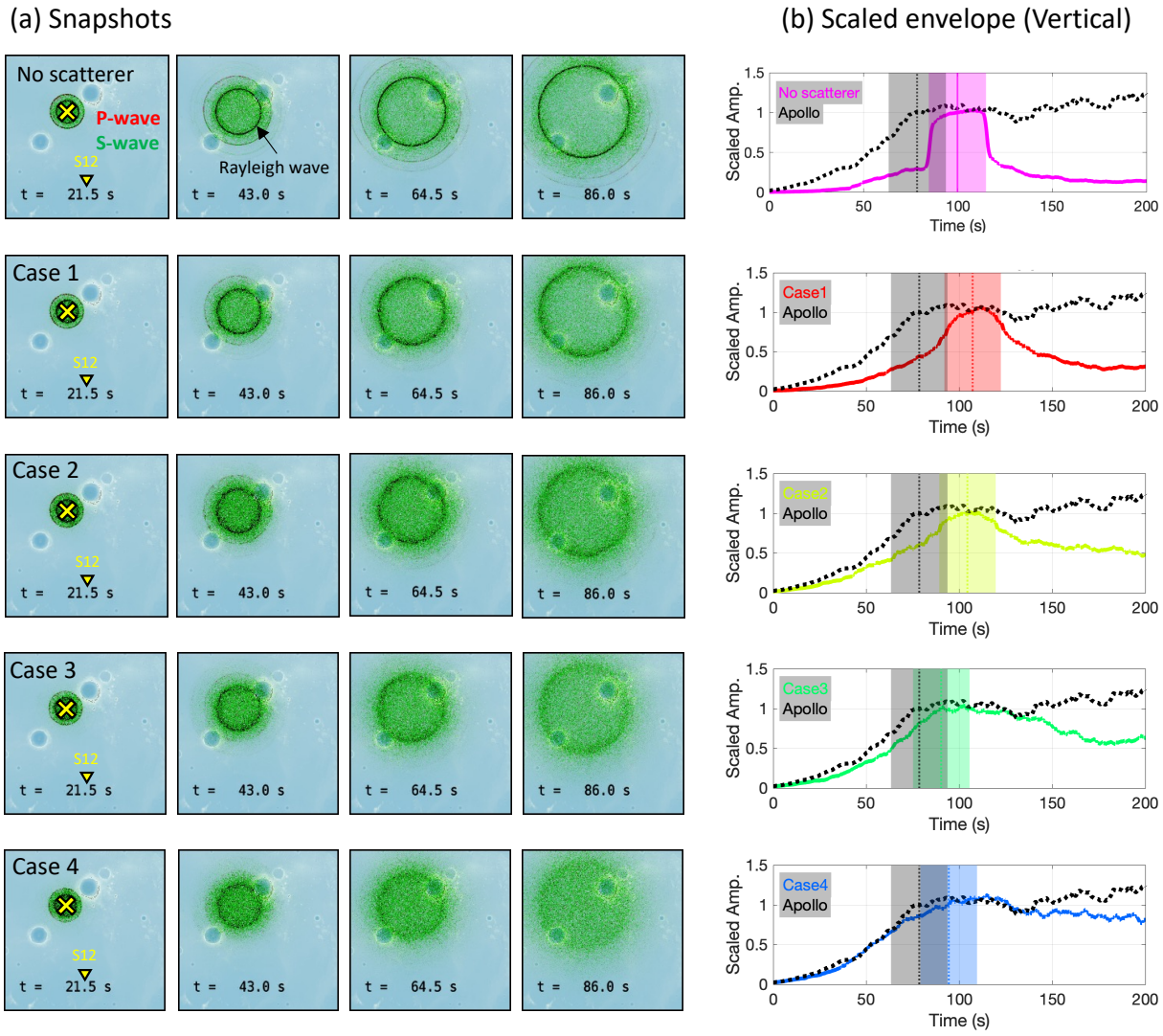

Figure 5. (a) Snapshots of each simulation on the horizontal plane. The time evolutions of wave propagation for Case 1 through Case 4 are shown from the second row to the bottom. Note that the simulation result without random media is shown at the top as a reference. The yellow cross shows the location of the source (Apollo 16 SIVB impact) and the seismic station (Station 12). The red wave corresponds to the compressional component and the green to the shear component. In this case, the random media displayed in Figure 3b are inserted in the first 5 km. The snapshots for the vertical cross sections are found in Figure S5 through S9 in Supporting Information. Note that the absorption layer (Perfectly Matched Layer; Zhang and Shen, 2010) is inserted at the boundary to suppress artificial reflections. An example of snapshots for longer duration can be found in Figure S10. (b) Comparison of smoothed envelopes of the vertical component between the Apollo and synthetics for the respective cases. All results are filtered between 0.3 – 1.5 Hz, then smoothed with a 30 s time window and 50% overlap. The black curve corresponds to the Apollo data and the colored ones to the synthetics. The vertical lines with shade represent the peak energy (rise-time) arrivals and their error ranges. The error bar follows the window size for smoothing. The amplitudes are normalized with the value at the respective rise-times.

More quantitative comparison between the observations and synthetics was made by measuring the rise-time and EED (Figure 6a-c). While Case 1 and 2 are plotted far away from the Apollo, the intense scattering cases (Case 3 and 4) are in accordance with the observation. Moreover, looking at the results of the amplitude ratio (Figure 6d), we clearly observe that the ratio gets closer to the observation as the scattering gets stronger — meaning that the envelope shape changes from peaked-shape to flat one as seen

in Figure 5b. From these results, we conclude Case 4 is preferable as a base model for the further investigations in the following sections.

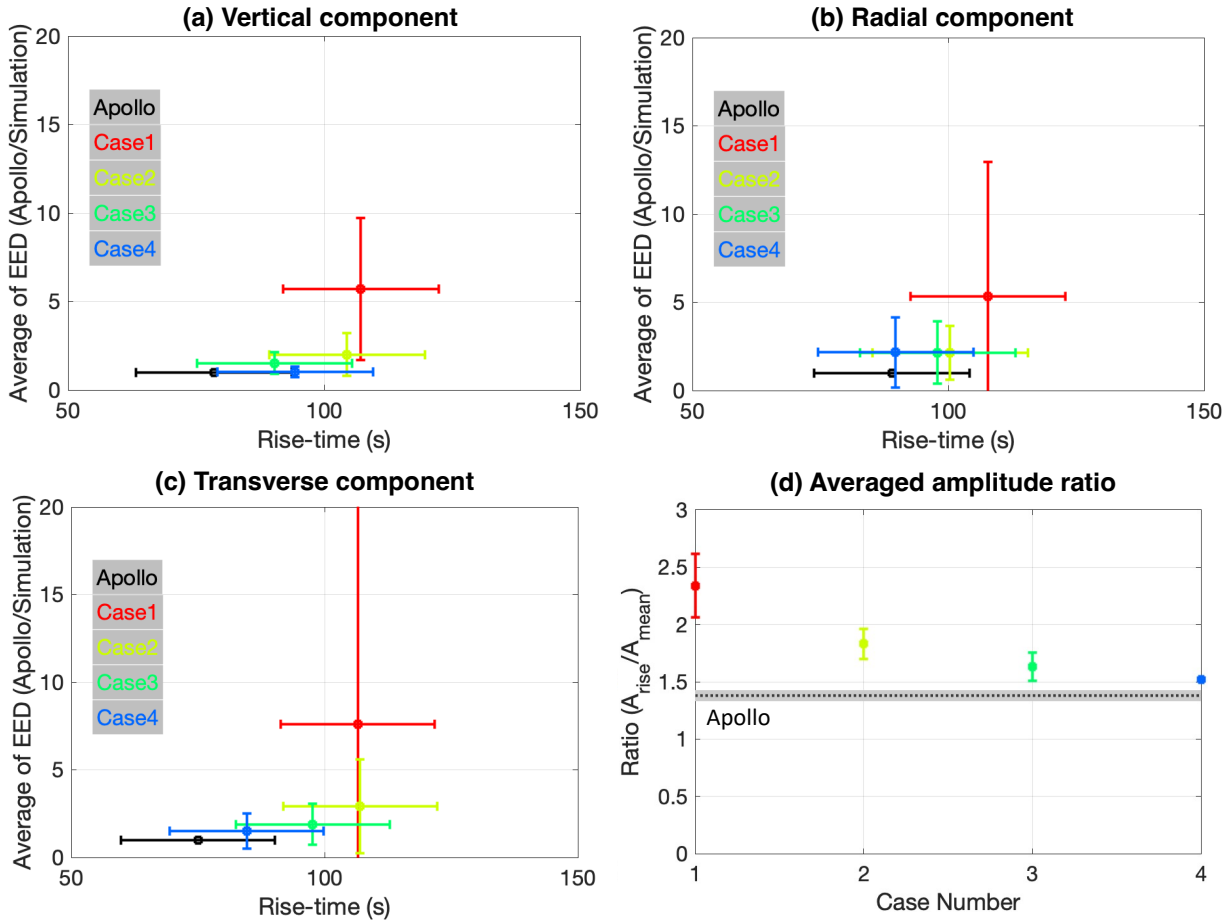

Figure 6. Rise-time versus equivalent energy density ratio (EED ratio) for (a) the vertical, (b) the radial, and (c) the transverse components. The black plots show the Apollo, and the colored are for respective simulation cases. The horizontal axis shows the rise-time with error of ±15 s. The vertical axis shows the average value of the EED ratio between the observation and synthetics over $2T_{rise}$ with standard deviation. (d) Results of the amplitude ratio values. The colored plots with error bars show the averaged values of the vertical, radial, and transverse components. The black dotted lines are the amplitude ratio values for the Apollo data with error range.

3.2 Application of the estimated scattering model to Apollo 14 SIVB impact

To observe whether Case 4 — the best model for the Apollo 16 SIVB impact — can also explain the other event, we performed another simulation for the Apollo 14 SIVB impact under the same parameter settings. Figure 7 compares the simulated envelopes with the Apollo ones. Overall, the envelope shape shows similar features to the data. The rise-time is in accordance with the error range for all components, and the amplitude ratio averaged using the three components takes the value of 1.59 ± 0.10 close to that of the Apollo (1.30 ± 0.05). However, making a comparison with the Case 4 results for the Apollo 16 SIVB impact (i.e., Figure 5b and Figure 7a), it does not seem that the fitting and the consistency of energy trend is as good as that for the Apollo 16 SIVB case. In the following section, we give some modifications to the Case 4 structure to see what kind of model can improve the results.

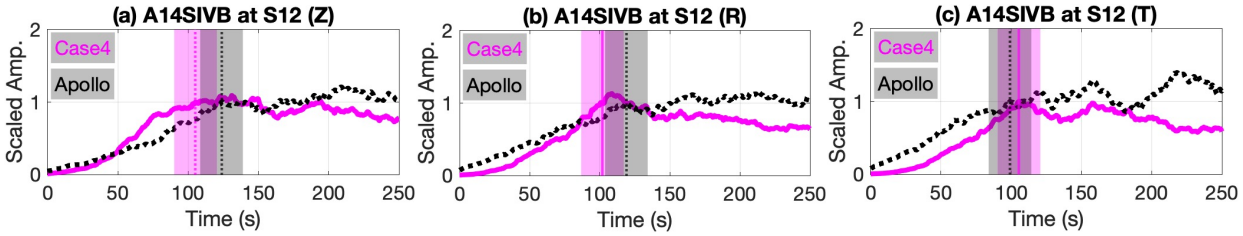

Figure 7. Smoothed envelopes of Apollo 14 SIVB impact observed at Station 12 in (a) the vertical, (b) the radial, and (c) the transverse components. The black envelopes are for the Apollo data, and the magenta profiles are for the simulation assuming Case 4 structure. The vertical lines with shade show the rise-time arrivals with error ranges. All envelopes are normalized with the value at each rise-time.

3.3 Modification of the vertical scattering structure

To improve the simulation results for the Apollo 14 SIVB impact case, we modify the vertical scattering structure. Since the computation is expensive (28 TB total memory for each run), we prepared three different structures to roughly confirm what kind of structure improves the synthetics. The assumed structures (Case 4α, β, and γ) are shown in Figure 8a. Among these models, Case 4α shows a gradual decrease in velocity fluctuation. In Case 4β, the scattering gets rapidly weak at 3.5 km (i.e., thin intense scattering). Case 4γ keeps the intense scattering layer down to 10 km, then rapidly turns into a more consolidated structure below that depth.

The simulation results are displayed in Figure 8b-d. Looking at the vertical components, there is little difference between the three cases. On the other hand, some differences are observed in the horizontal components. For example, while the rise-times of Case 4β and γ (blue and green) coincide with the data within the error bars, the transverse component of Case 4α (red) does not. From the comparison between Case 4α with the rest of the two, it does not seem that the gradually changing structure is suitable for the Apollo 12 landing site.

Concerning the preference between the thin (Case 4β) or the thick scattering layer (Case 4γ), Case 4γ is more similar to the observation, which can be confirmed from the averaged amplitude ratio in Figure 9. In fact, Case 4γ also works well for Apollo 16 SIVB impact (Figure 10). Thus, the intense scattering appears to continue down to 10 km at least at the Apollo 12 landing site.

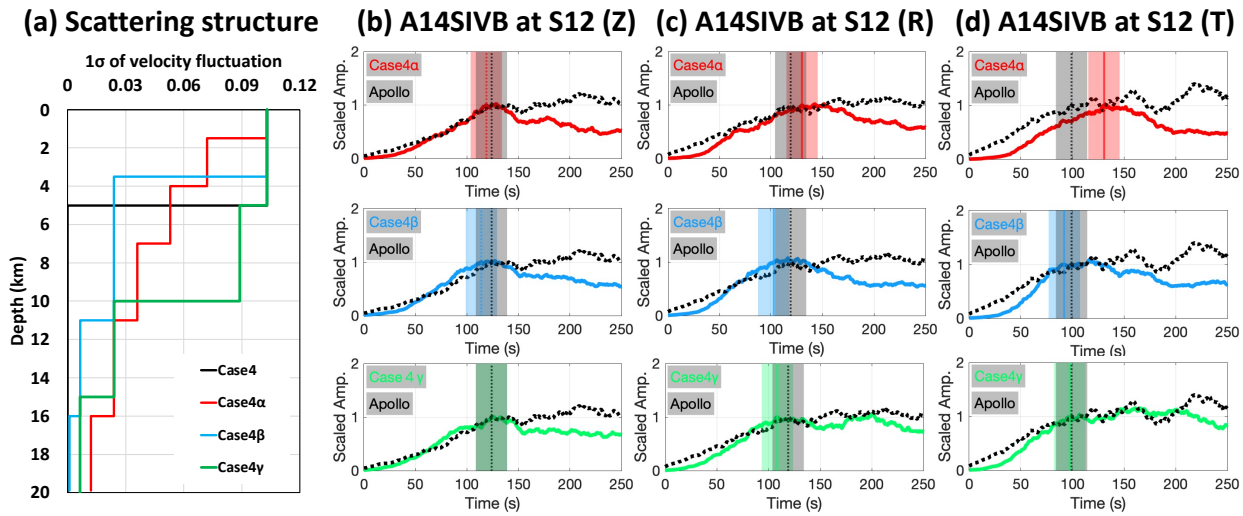

Figure 8. (a) Assumed scattering structures. The black line is Case 4 which was used in the previous section. The red, blue, and green are Case 4α, β, γ, respectively. (b)-(d) The comparisons between the simulation results (colored) with the Apollo data (black) for the vertical, radial, and transverse components from left to right. The first row is for Case 4α, followed by Case 4β, and Case 4γ. The vertical lines with shade represent the rise-times with their error ranges.

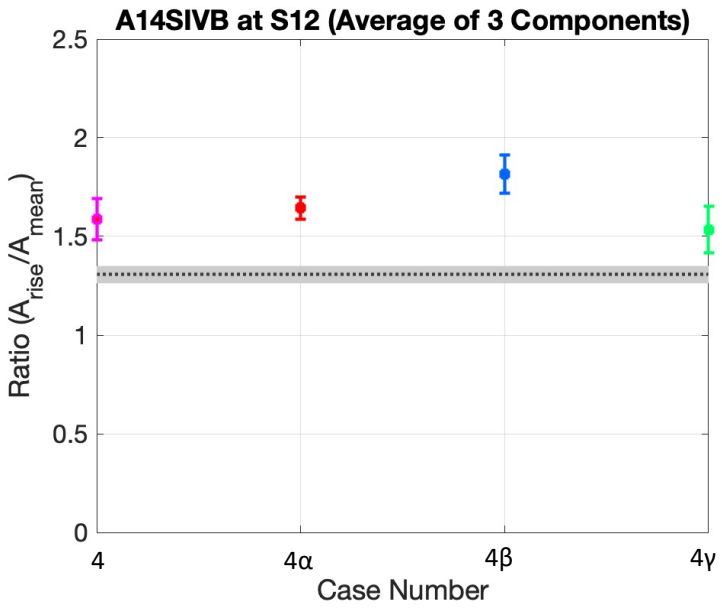

Figure 9. Averaged amplitude ratios of the three components (radial, transverse, and vertical). Magenta plot is for Case 4, red for Case 4α, blue for Case 4β, and green for Case 4γ.

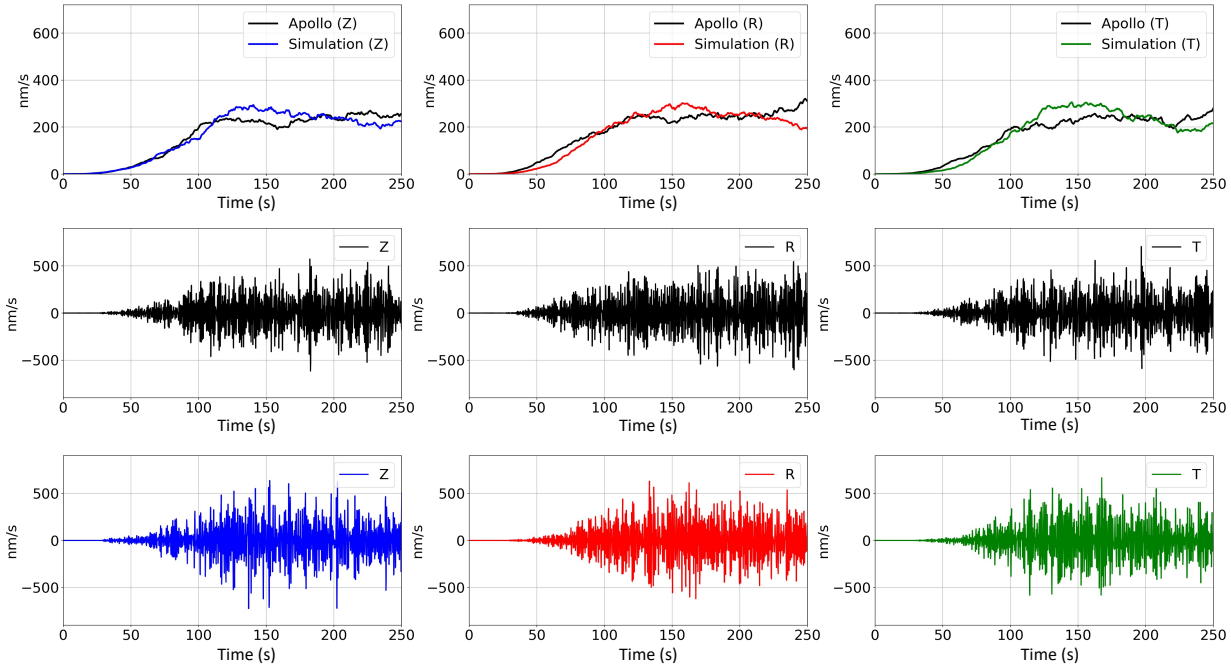

Figure 10. The results for Apollo 16 SIVB impact for Case 4 γ. (Top row) Comparisons of smoothed envelopes between the Apollo (black) and the simulation (colored). (Middle row) The vertical, radial, and transverse waveforms of the Apollo data from the left to right. The waveforms are filtered between 0.3 and 1.5 Hz. (Bottom row) Simulated waveforms in nm/s. The vertical, radial, and transverse components are shown from the left to right. The waveforms are filtered between 0.3 and 1.5 Hz.

4 Discussion

4.1 Interpretation of the derived structure

From the forward modeling, we found that the 10 km intense scattering model (Case 4γ) best explains the observations. The structural transition at 10 km depth was actually expected in previously proposed models (Hawke et al., 2003; Yamamoto et al., 2012), although that is more related to the compositional transition from the mafic-rich materials into the plagioclase-rich anorthosite. It is also pointed out that the mafic-rich layer has compositional variations due to the continuous meteoroid impacts in the early history of the Moon (Hawke et al., 2003). From another aspect, the numerical simulation of the spatial development of impact fragments by Wiggins et al. (2019) showed that the fragmentations with several hundreds of meters — which affect the seismic wave propagation — could develop down to 5 km from the surface. Putting together these pieces of information with our model, within the 10 km scattering layer, the first several-km layer reflects the structural fragmentation and more reflects the compositional variations below that; then the structure turns into a massive plagioclase-rich crust where the composition and physical structure get more homogeneous at around 10 km depths.

4.2 Comparison between the Earth, Mars, and the Moon in terms of scattering and attenuation environment

The quantified scattering parameter enables us to compare the scattering environment between the Earth, Mars, and the Moon. Figure 11a compares the three solid bodies from the viewpoint of seismic scattering, where the intensity of scattering is evaluated with scattering attenuation factor Q_s defined as:

$$Q_s^{-1} = \frac{n_s}{k_s} \qquad (8)$$

where n_s is the scattering coefficient corresponding to the reciprocal of the mean free path between scattering media. Here, we regarded the correlation length as the mean free path. k_s is wavenumber for a given frequency, that is:

$$k_s = \frac{2\pi f}{V} \qquad (9)$$

where f refers to the frequency — ranging from 0.3 to 1.5 Hz — and V is the seismic wave velocity (S-wave velocity in the megaregolith layer in this study). The smaller Q_s value (i.e., larger Q_s^{-1}) means more intense scattering. In Figure 11a, the lunar and Martian Q_s (colored filled area) are superposed on those evaluated at various sites on the Earth (Sato et al., 2012 and references therein).

Paying attention to the terrestrial Q_s^{-1}, it ranges from 10^{-1} to 10^{-5} in the lithosphere and does from 5×10^{-3} to 10^{-4} in the mantle. The volcanic region, whose subsurface structure is heterogenous, shows a relatively high value of 10^{-2} compared to the typical values for the lithosphere. Turning to Mars, the first results from the InSight (Interior Exploration using Seismic Investigations, Geodesy and Heat Transport) mission (Lognonné et al., 2020 and Menina et al., 2021) show a similar value to those observed in the terrestrial lithosphere. Two filled areas are displayed for the Moon: one is estimated based on the radiative transfer modeling (Gillet et al., 2017) and the other is through our numerical simulation. Gillet et al. (2017) analyzed various types of moonquakes besides meteoroid impacts, whose excited waves are sensitive to the subsurface heterogeneity, and estimated the global structure of Q_s (the crustal value is presented in Figure 11a). On the other hand, our research focuses on the closely located impacts, which are suitable for investigating megaregolith — the most heterogeneous region on the Moon. While the lunar crustal Q_s^{-1} is comparable with the most inhomogeneous region on the Earth displayed, the lunar megaregolith Q_s^{-1} shows a higher value than those measured on the Earth and Elysium Planitia on Mars, suggesting the uppermost part of the Moon is highly heterogeneous.

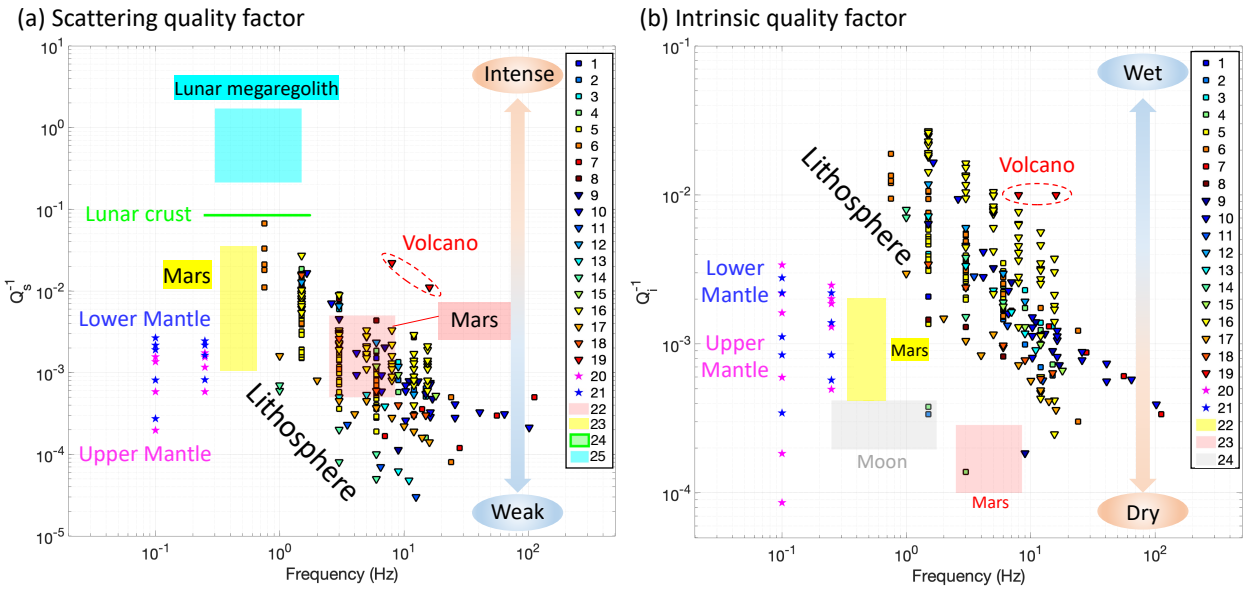

Figure 11. (a) Comparison of scattering attenuation factor between the Earth, Mars, and the Moon. The horizontal axis shows frequency and the vertical shows the inverse value of the scattering attenuation factor. The larger Q_s^{-1} shows the more intense scattering. For the terrestrial case, results for a variety of areas are plotted. The red and yellow hatched areas are the first results of Elysium Planitia on Mars in the InSight mission. The green-filled area shows the previous estimate for the lunar crust and the cyan area shows our result for the lunar megaregolith. The numbers in the legend correspond to the references summarized in Table S6. (b) Comparison of intrinsic attenuation factor between the Earth, Mars, and the Moon. The larger Q_i^{-1} shows the larger attenuation, implying that the medium holds more fluid. As in (a), the results for various fields on the Earth and Elysium Planitia on Mars, the crust, and/or mantle of the Moon are shown together. The numbers in the legend correspond to the references summarized in Table S7.

Our results arise a question; why does the Moon show more intense scattering than others? The answer can be explained by the difference in gravity conditions. It is known that the compressional pressure increases more rapidly under larger gravity conditions. In other words, the critical depth — where the plastic deformation stops — is located shallower as the planet's size gets larger, making it harder for impact fragments to develop (Wiggins et al., 2019). In addition, the existence of an atmosphere plays an important role in the surface evolution of a solid body. With an atmosphere, the impact velocity would be decelerated, resulting in smaller impact energy. Thus, it is reasonable that the Moon has a much more heterogeneous structure because of its small size and the lack of an air shield against continuous meteoroid impacts over several billion years.

Another comparison is made in Figure 11b where the intrinsic attenuation factor Q_i is compared between the three bodies. The smaller Q_i (i.e., larger Q_i^{-1}) indicates that the seismic energy attenuates more rapidly, generally implying that the medium includes more fluid. On Earth, large Q_i^{-1} ($\sim 10^{-2}$) is obtained at geologically active regions (e.g., volcanic front, active fault) (e.g., Sato et al., 2012). In the case of the Moon and Mars, much lower Q_i^{-1} values are obtained, indicating they are in an extremely dry environment, especially compared to the terrestrial lithosphere. This is consistent with a general view of the respective planetary environments. Combining these facts with Q_s results makes it easier to interpret the differences in the seismic observations on each body. Since the Moon is in extremely heterogenous and low attenuation conditions, the seismic waves are highly scattered with less absorption, making the seismic phases unclear and prolonging the event duration. Mars shows a dry environment, but the scattering factor is comparable with that of the Earth's lithosphere. This explains why marsquakes have a longer duration than those on Earth with less diffused phase arrivals (such as P, S) than moonquakes (Lognonné et al., 2020).

5 Conclusions

In this study, we accomplished the first reproduction of the intensely scattered seismic waves observed on the Moon through the full 3D seismic wave propagation simulation. This allowed us to make significant progress in understandings of scattering properties of the most heterogeneous region of the Moon (megaregolith), which has been a long-standing problem since lunar seismology started.

The quantified scattering parameters are compared with those evaluated on other planets, helping us interpret the different characteristics observed in seismic waves on each solid body. Since the seismic scattering is a common feature seen in planetary seismology, our approach would be helpful in investigating any other solid planetary bodies in future explorations.

To summarize, our study not just shed light on one of the most complicated problems in lunar seismology but also opened a new way for comparative planetology in terms of seismic scattering, which is expected to give us a paramount key to further understanding of how a planetary surface evolved since its formation.

Acknowledgments

We appreciate Japan Agency for Marine-Earth Science and Technology (JAMSTEC) for providing us with computational resources (the Earth Simulator). We thank Dr. Makiko Ohtake of University of Aizu and Dr. Hiroshi Nagaoka of RIKEN for giving us constructive advice from the viewpoint of the geochemical evolution of the Moon. We acknowledge NASA, CNES, their partner agencies and Institutions (UKSA, SSO, DLR, JPL, IPGP-CNRS, ETHZ, IC, MPS-MPG) and the flight operations team at JPL, SISMOC, MSDS, IRIS-DMC and PDS for providing SEED SEIS data. We also would like to show our gratitude to editor Laurent Montési and two reviewers for their constructive comments on our manuscript, which helped us make our results and conclusions more solid. This work was supported in part by The Graduate University for Advanced Studies, SOKENDAI.

Data Availability

The Apollo seismic data used in this study were collected from the Data Archives and Transmission System (DARTS) by the Center for Science-satellite Operation and Data Archive (C-SODA) of the Institute of Space and Astronautical Science of the Japan Aerospace Exploration Agency (https://darts.isas.jaxa.jp/planet/seismology/apollo/index.html). Simulation outputs are available at Onodera (2022). The simulation source code (OpenSWPC) is provided by Maeda et al. (2017) available at Maeda (2020). The maps were made with the Generic Mapping Tool (GMT; Wessel et al., 2019). The InSight seismic data used in this study can be retrieved through InSight Mars SEIS data Service (2019).

References

- Aki (1969), Analysis of seismic coda of local earthquakes as scattered waves, *J. Geophys. Res.*, 74, 615 – 631.
- Aki and Chouet (1975), Origin of coda waves: source, attenuation and scattering effect, *J. Geophys. Res.*, 80. 3322 – 3342.
- Araki, H., Tazawa, S., Noda, H., Ishihara, Y., Goossens, S., Sasaki, S. et al. (2009), Lunar Global Shape and Polar Topography Derived from Kaguya-LALT Laser Altimetry, *Science*, 323, 897-900, https://www.science.org/doi/10.1126/science.1164146.
- Barker, M. K., Mazarico, E., Neumann, G. A., Zuber, M. T., Haruyama, J., Smith, D. E. (2016), A new lunar digital elevation model from the lunar orbiter laser altimeter and SELENE terrain camera, *Icarus, 273*, 346-355, https://doi.org/10.1016/j.icarus.2015.07.039.
- Besserer, J., Nimmo, F., Wieczorek, M. A., Weber, R. C., Kiefer, W. S., McGovern, P. J., Andrews-Hanna, J. C., Smith, D. E., and Zuber, M. T. (2014), GRAIL gravity constraints on the

vertical and lateral density structure of the lunar crust, *Geophys. Res. Lett.*, 41, 5771– 5777, doi:10.1002/2014GL060240.

- Dainty, A. M., Toksöz, M. N., Anderson, K. R., Pines, P. J., Nakamura, Y., Latham, G. (1974), Seismic scattering and shallow structure of the Moon in Oceanus Procellarum, *The Moon*, 9, 11-29.
- Dainty, A. M. and Toksöz, M., N. (1981), Seismic coda on the Earth and the Moon: a comparison, *Phys. Earth Planet. Int., 26*, 250-260, https://doi.org/10.1016/0031-9201(81)90029-7.
- Garcia, R.F., Khan, A., Drilleau, M. *et al.* Lunar Seismology: An Update on Interior Structure Models. *Space Sci Rev* **215,** 50 (2019). https://doi.org/10.1007/s11214-019-0613-y.
- Gagnepain-Beyneix, J., Lognonné, P., Chenet, H., Lombardi, D., Spohn, T. (2006), A seismic model of the lunar mantle and constraints on temperature and mineralogy, Phys. Earth Planet. Int., 159, 140-166.
- Gillet, K., Margerin, L., Calvet, M., Monnereau, M. (2017), Scattering attenuation profile of the Moon: implications for shallow moonquakes and the structure of the megaregolith, *Phys. Earth Plant. Int., 262*, 28-40, https://doi.org/10.1016/j.pepi.2016.11.001.
- Hawke, B. R., Peterson, C. A., Blewett et al. (2003), Distribution and modes of occurrence of lunar anorthosite, *J. Geophys. Res.*, 108, 5050, doi:10.1029/2002JE001890, E6.
- InSight Mars SEIS data Service (2019). SEIS raw data, InSight mission. IPGP, JPL, CNES, ETHZ, ICL, MPS, ISAE-Supaero, LPG, MSFC, https://doi.org/10.18715/SEIS.INSIGHT.XB_2016
- Karakostas, F., Schmerr, N., Maguire, R., Huang, Q., Kim, Q., Lekic, V., Margerin, L., Nunn, C., Menina, S., Kawamura, T., Lognonné, P., Giardini, D., Banerdt, B. (2021), Scattering attenuation of the Martian interior through coda-wave analysis, *Bulletin of the Seismological Society of America*, 111 (6), 3035–3054.
- Latham, G. et al. (1970), Seismic data from man-made impacts on the Moon, *Science, 170*, 3958, 620-626, doi: 10.1126/science.170.3958.620.
- Lognonné, P., Banerdt, W.B., Pike, W.T. *et al.* (2020), Constraints on the shallow elastic and anelastic structure of Mars from InSight seismic data. *Nat. Geosci.* **13,** 213–220, https://doi.org/10.1038/s41561-020-0536-y.
- Maeda, T., Takemura, S. & Furumura, T. (2017). OpenSWPC: an open-source integrated parallel simulation code for modeling seismic wave propagation in 3D heterogeneous viscoelastic media. *Earth Planets Space* **69,** 102, https://doi.org/10.1186/s40623-017-0687-2.
- Maeda. T. (2020). tktmyd/OpenSWPC: Version 5.1.0, Zenodo, https://doi.org/10.5281/zenodo.3982232
- Menina, S., Margerin, L., Kawamura, T., Lognonné, P., Marti, J. et al. (2021), Energy envelope and attenuation characteristics of high frequency (HF) and very-high-frequency (VF) Martian events, *Bull, Seismol. Soc. Am., 111*, 6, 3016–3034, https://doi.org/10.1785/0120210127.
- Mizutani, H., Osako, M. (1974), Elastic-wave velocities and thermal diffusivities of Apollo 17 rocks and their geophysical implications, Proc. Lunar Sci. Conf., 5*t*h, 2891-2901.
- Nakamura, T., Takenaka, H., Okamoto, T., Kaneda, Y. (2012), FDM simulation of seismic-wave prop- agation for an aftershock of the 2009 Suruga bay earthquake: effects of ocean-bottom topography and seawater layer, *Bull. Seismol. Soc. Am., 102*, 2420-2435, https://doi.org/10.1785/0120110356.
- Oberst, P. J. (1989), Meteoroids near the Earth-Moon system as inferred from temporal and spatial distribution of impacts detected by the lunar seismic network, PhD dissertation, The University of Texas at Austin.
- Onodera, K., Kawamura, T., Tanaka, S., Ishihara, Y., and Maeda, T. (2021). Numerical simulation of lunar seismic wave propagation: Investigation of subsurface scattering properties near Apollo 12 landing site. *Journal of Geophysical Research: Planets*, 126, e2020JE006406. https://doi.org/10.1029/2020JE006406.
- Onodera, K. (2022), Onodera0726/JGR_Onodera_2022, GitHub Data Repository, https://doi.org/10.5281/zenodo.7151401.

- Rajšić, A., Miljković, K., Wójcicka, N., Collins, G. S., Onodera, K., Kawamura, T., et al. (2021). Numerical simulations of the Apollo S-IVB artificial impacts on the Moon. *Earth and Space Science*, *8*, e2021EA001887. https://doi. org/10.1029/2021EA001887
- Sato (1977), Energy propagation including scattering effect. Single isotropic scattering approximation, *J. Phys. Earth*, 25, 27 – 41.
- Sato, H. and Fehler, M. (1998) Seismic wave propagation and scattering in the heterogeneous Earth, AIP Press/Springer, New York.
- Sato, H., Fehler, M. C., Maeda, T. (2012), Seismic wave propagation and scattering in the heterogeneous Earth, *2nd edn*, Springer, Berlin.
- Shiomi, K., Sato, H., Ohtake, M. (1997) Broad-band power-law spectra of well-log data in Japan, *Geophys. J. Int., 130*, 57–64, https://doi.org/10.1111/j.1365-246X.1997.tb00987.x.
- Sivaji, C., Nishizawa, O., Kitagawa, G., Fukushima, Y. (2002), Aphysical-model study of the statistics of seismic waveform fluctuations in random heterogeneous media, Geophys. J. Int., 148, 575-595.
- Sondergeld, C. H., Granryd, L. A., Spetzler, H. A. (1979), Compressional velocity measurements for a highly fractured lunar anorthosite, *Prc. Lunar Planet. Sci. Conf., 10*th, 2147-2154.
- Suzuki, H., Ikeda, R., Mikoshiba, T., Kinoshita, S., Sato, H., Takahashi, H. (1981), Deep well logs in the Kanto-Tokai area (in Japanese), Rev. Nat. Res. Ctr. Disast. Prev., 65, 1–162.
- Wessel, P., Luis, J. F., Uieda, L., Scharroo, R., Wobbe, F., Smith, W. H. F., & Tian, D. (2019). The Generic Mapping Tools version 6. *Geochemistry, Geophysics, Geosystems*, 20, 5556– 5564. https://doi.org/10.1029/2019GC008515.
- Wieczorek, M. A., Neumann, G. A., Nimmo, F., Kiefer, W. R., Taylor, G. J., Melosh, H. J., The crust of the Moon as seen by GRAIL, *Science*, *339*, 6120, 671-675, DOI: 10.1126/science.1231530.
- Wiggins, S. E., Johnson, B. C., Bowling, T. J., Melosh, H. J., & Silber, E. A. (2019). Impact fragmentation and the development of the deep lunar megaregolith. *Journal of Geophysical Research: Planets*, 124, 941– 957. https://doi.org/10.1029/2018JE005757.
- Wu (1985), Multiple scattering and energy transfer of seismic waves – separation of scattering effect from intrinsic attenuation – II. Application of the theory to Hindu-Kush region, *Pure Appl. Geophys.*, 128, 49 – 80.
- Yamamoto, S., Nakamura, R., Matsunaga et al. (2012), Massive layer of pure anorthosite on the Moon, *Geophys. Res. Lett.*, 39, L13201, doi:10.1029/2012GL052098.
- Zhang W, Shen Y (2010), Unsplit complex frequency-shifted PML implementation using auxiliary differential equations for seismic wave modeling. Geophysics 75:T141–T154. doi:10.1190/1.3463431.

References from the Supporting Information

- Adams, D.A. and Abercrombie, R.E. (1998), Seismic attenuation above 10 Hz in southern California from coda waves recorded in the Cajon Pass borehole, *J. Geophys. Res.*, 103:24, 257–24, 270, https://doi.org/10.1029/98JB01757.
- Akinci, A, Pezzo, E.D., Ibanez, J.M. (1995), Separation of scattering and intrinsic attenuation in southern Spain and western Anatolia (Turkey), *Geophys. J. Int.*, 121:337–353, https://doi.org/10.1111/j.1365-246X.1995.tb05715.x.
- Akinci, A. and Eyidogan, H. (2000), Scattering and anelastic attenuation of seismic energy in the vicinity of north Anatolian fault zone, eastern Turkey, *Phys. Earth Planet. Inter.*, 122:229–239, https://doi.org/10.1016/S0031-9201(00)00196-5.
- Bianco, F., Pezzo, E.D., Castellano, M., Ibanez, J., Luccio, F.D. (2002), Separation of intrinsic and scat- tering seismic attenuation in the Southern Apennine zone, Italy, *Geophys. J. Int.*, 150(1):10–22, https://doi.org/10.1046/j.1365-246X.2002.01696.x.
- Bianco, F., Pezzo, E.D., Malagnini, L., Luccio, F.D., Akinci, A. (2005), Separation of depth-dependent intrinsic and scattering seismic attenuation in the northeastern sector of the Italian Peninsula. *Geophys. J. Int.*, 161(1):130–142, https://doi.org/10.1111/j.1365-246X.2005.02555.x.

- Blanchette-Guertin, J.-F., Johnson, C. L., and Lawrence, J. F. (2012), Investigation of scattering in lunar seismic coda, *J. Geophys. Res.*, 117, E06003, doi:10.1029/2011JE004042.
- Blanchette-Guertin, J. F., Johnson, C. L., and Lawrence, J. F. (2015), Modeling seismic energy propagation in highly scattering environments. *J. Geophys. Res. Planets*, 120, 515– 537. doi: 10.1002/2014JE004654.
- Daubar, I. J., Lognonné, P., Teanby, N. A., Collins, G. S., Clinton, J., Stahler, S. et al. (2020), A new crater near InSight: Implications for seismic impact detectability on Mars, *J. Geophys. Res.: Planets*, 125, e2020JE006382, https://doi.org/10.1029/2020JE006382.
- Dutta, U., Biswas, N., Adams, D., Papageorgiou, A. (2004), Analysis of S-wave attenuation in South- Central Alaska, *Bull. Seism. Soc. Am.*, 94(1):16–28, https://doi.org/10.1785/0120030072.
- Fehler, M., Hoshiba, M., Sato, H., Obara, K. (1992), Separation of scattering and intrinsic attenuation for the Kanto-Tokai region, Japan, using measurements of S-wave energy versus hypocentral distance, *Geophys. J. Int.*, 108:787–800, https://doi.org/10.1111/j.1365-246X.1992.tb03470.x.
- Garcia, R. F., Gagnepain-Beyneix, J., Chevrot, S., Lognonné, P. (2011), Very preliminary reference Moon model, *Phys. Earth Planet. Int., 188*, 96-113, https://doi.org/10.1016/j.pepi.2011.06.015.
- Giampiccolo, E., Tuve, T., Gresta, S., Patane, D. (2006), S-waves attenuation and separation of scattering and intrinsic absorption of seismic energy in southeastern Sicily (Italy), *Geophys. J. Int.*, 165:211–222, https://doi.org/10.1111/j.1365-246X.2006.02881.x.
- Goutbeek, F.H., Dost, B., van Eck, T. (2004), Intrinsic absorption and scattering attenuation in the southern part of the Netherlands, *J. Seis.*, 8:11–23, https://doi.org/10.1023/B:JOSE.0000009511.27033.79.
- Gudkova, T. V., Lognonné, P., and Gagnepain-Beyneix, J. (2011). Large impacts detected by the Apollo seismometers: Impactor mass and source cutoff frequency estimations. *Icarus*, *211*(2), 1049–1065. https://doi.org/10.1016/j.icarus.2010.10.028
- Gudkova, T. V., Lognonné, P., Miljković, K., and Gagnepain-Beyneix, J. (2015). Impact cutoff frequency – Momentum scaling law inverted from Apollo seismic data. *Earth and Planetary Science Letters*, *427*, 57–65. https://doi.org/10.1016/j.epsl.2015.06.037
- Hatzidimitriou, P.M. (1994), Scattering and anelastic attenuation of seismic energy in northern Greece, *Pure Appl. Geophys.*, 143:587–601, https://doi.org/10.1007/BF00879499.
- Hoshiba, M. (1993), Separation of scattering attenuation and intrinsic absorption in Japan using the multiple lapse time window analysis of full seismogram envelope, *J. Geophys. Res.*, 98 (B9), 15809– 15824, doi:10.1029/93JB00347.
- Jin, A., Mayeda, K., Adams, D., and Aki, K. (1994), Separation of intrinsic and scattering attenuation in southern California using TERRAscope data, *J. Geophys. Res.*, 99(B9), 17835– 17848, doi:10.1029/94JB01468.
- Leary, P. and Abercrombie, R. (1994), Frequency dependent crustal scattering and absorption at 5−160 Hz from coda decay observed at 2.5 km depth, *Geophys. Res. Lett.*, 21:971–974, https://doi.org/10.1029/94GL00977.
- Lee, W. S., Sato, H., and Lee, K. (2003), Estimation of *S*-wave scattering coefficient in the mantle from envelope characteristics before and after the *ScS* arrival, *Geophys. Res. Lett.*, 30, 2248, doi:10.1029/2003GL018413, 24.
- Lee, W.S., Sato, H., Lee, K. (2006), Scattering coefficients in the mantle revealed from the seismogram envelope analysis based on the multiple isotropic scattering model, *Earth Planet. Sci. Lett.*, 241:888–900, https://doi.org/10.1016/j.epsl.2005.10.035.
- Lognonné, P., Gagnepain-Beyneix, J., Chenet, H. (2003), A new seismic model of the Moon: implications for structure, thermal evolution and formation of the Moon, *Earth Plant. Sci. Lett., 211*, 27-44, https://doi.org/10.1016/S0012-821X(03)00172-9.
- Mayeda, K., Koyanagi, S., Hoshiba, M., Aki, K., and Zeng, Y. (1992), A comparative study of scattering, intrinsic, and coda Q^{-1} for Hawaii, Long Valley, and central California between 1.5 and 15.0 Hz, *J. Geophys. Res.*, 97 (B5), 6643– 6659, doi:10.1029/91JB03094.

- Nakamura, Y., and Koyama, J. (1982), Seismic *Q* of the lunar upper mantle, *J. Geophys. Res.*, 87 (B6), 4855– 4861, doi:10.1029/JB087iB06p04855.
- Orloff (2000), Apollo by the numbers: a statistical reference, NASA SP-2000-4029.
- Teanby and Wookey (2011), Seismic detection of meteorite impacts on Mars, *Phys. Earth Planet. Int., 186*, 70-80, https://doi.org/10.1016/j.pepi.2011.03.004.
- Toksöz, M. N., Dainty, A. M., Solomon, S. C., and Anderson, K. R. (1974), Structure of the Moon, *Rev. Geophys.*, 12(4), 539– 567, doi:10.1029/RG012i004p00539.
- Ugalde, A., Pujades, L.G., Canas, J.A., Villasenor, A. (1998), Estimation of the intrinsic absorption and scattering attenuation in northeastern Venezuela (southeastern Caribbean) using coda waves, *Pure Appl. Geophys.*, 153:685–702, DOI: 10.1007/978-3-0348-8711-3_21.
- Vargas, C.A., Ugalde, A., Pujades, L.G., Canas, J.A. (2004), Spatial variation of coda wave attenuation in northwestern Colombia, *Geophys. J. Int.*, 158:609–624, https://doi.org/10.1111/j.1365-246X.2004.02307.x.
- Yamamoto, M., and Sato, H. (2010), Multiple scattering and mode conversion revealed by an active seismic experiment at Asama volcano, Japan, *J. Geophys. Res.*, 115, B07304, doi:10.1029/2009JB007109.
- Wagner, R. V., Nelson, D. M., Plescoa, J. B., Robinson, M. S., Speyerer, E. J., Mazarico, E. (2017), Coordinates of anthoropogenic features on the Moon, *Icarus, 283*, 92-103, https://doi.org/10.1016/j.icarus.2016.05.011.

Geophysical Research Letters

Supporting Information for

Quantitative evaluation of the lunar seismic scattering and comparison between the Earth, Mars, and the Moon

K. Onodera[1,2,3], T. Kawamura[2], S. Tanaka[4], Y. Ishihara[5], T. Maeda[6]

[1]Earthquake Research Institute, The University of Tokyo, Tokyo, Japan.

[2]Université Paris Cité, Institut de Physique du Globe de Paris, CNRS, Paris, France.

[3]The Graduate University for Advanced Studies, SOKENDAI, Kanagawa, Japan.

[4]Institute of Space and Astronautical Sciences, Japan Aerospace Exploration Agency, Kanagawa, Japan.

[5]JAXA Space Exploration Center (JSEC), Japan Aerospace Exploration Agency, Kanagawa, Japan.

[6]Graduate School of Science and Technology, Hirosaki University, Aomori, Japan.

Contents of this file

Introduction

This document includes the supplementary information about the detailed configuration of numerical simulations, the topography models, and the parameter studies concerning correlation length. Also, some figures and tables are included in to help readers better understand the contents of the main text.

Supporting Texts

Text S1. Configuration for numerical simulations

To realize a stable wave-propagation simulation up to 2.0 Hz, the parameters are optimized using a tool provided in the OpenSWPC (called "fdmcond.x"). It returns us the reasonable parameters for a computation we want to perform by evaluating the "wavelength condition" and "stability condition" (Maeda et al., 2017). The wavelength condition is related to the spatial resolutions (d_X,d_Y,d_Z), requiring that the grid number is at least 5 – 10 for a wavelength. The stability condition is related to both spatial and temporal resolution. In N_D-dimensional space for the p-order finite difference method, the condition is defined as:

$$dt \leq \frac{\left(\sum_{p=1}^{P/2} C_p\right)^{-1}}{V_{max}} \left(\sum_{i=1}^{N_D} \frac{1}{d_{x_i}^2}\right)^{-1/2} \quad \text{(S1)}$$

where V_{max} is the maximum velocity within a medium, C_p is the coefficient of the finite difference formula (C_1 = 9/8 and C_2 = 1/24 for 4th order accuracy in space as in this study), and d_{xi} is the spatial resolution (or spatial grid width) in *i*-th direction. The parameters for the numerical simulations are summarized in Table S4, and the corresponding workspaces are visualized in Figure 2 in the main text.

Text S2. Determination of ξ value

In order to determine the empirical constant ξ in Equation 4 in the main text, we computed the travel time for the two target artificial impacts. One is Apollo 16 SIVB impact recorded at Station 12 and the other is Apollo 14 SIVB impact observed at Station 12 (Figure 2 in the main text). The epicentral distances are 153.76 km and 175.34 km, respectively. Let us consider a stratified half-space where L is the epicentral distance, H_i and v_i represent the layer thickness and P-wave velocity at the *i*-th layer, respectively. θ_i is a critical angle at the *i*-th layer. According to Snell's law, $\theta_i = \arcsin(v_i/v_{i+1})$. In the case of the direct wave, the travel time t_{dir} can be computed as:

$$t_{dir} = L/v_i \quad \text{(S2)}$$

The travel time for refracted wave (t_{ref}) can be estimated considering the shortest path from the seismic source to the station through the underground. When $L > \sum_{i=1}^{N} 2H_i tan\theta_i$, t_{ref} can be expressed using the critical angles at respective boundaries like:

$$t_{ref} = 2\left[\sum_{i=1}^{N} \frac{H_i}{v_i cos\theta_i} + \left(\frac{L}{2} - \sum_{i=1}^{N} H_i tan\theta_i\right)/v_{i+1}\right] \quad \text{(S3)}$$

As $cos\theta_i = (1 - v^2{}_i / v^2{}_{i+1})^{1/2}$ and $tan\theta_i = v_i\,(v^2{}_{i+1} - v^2{}_i)^{-1/2}$, Equation S3 becomes

$$t_{ref} = 2\left[\sum_{i=1}^{N} \frac{H_i}{v_i\sqrt{1-(v_i/v_{i+1})^2}} + \left(\frac{L}{2} - \sum_{i=1}^{N} \frac{H_i}{\sqrt{v_{i+1}^2+v_i^2}}\right)/v_{i+1}\right] \quad \text{(S4)}$$

Travel times for several structure models shown in Figure S1 were computed using Equation S2 or S4. Figure S2 displays the computed travel times for various structure models (ξ = 2.0 – 24). The dotted lines show the estimated range of travel times for respective artificial impacts by Lognonné et al. (2003). Note that while the reading error of P-wave arrival is about 1 s for both events, Apollo 16 SIVB impact includes an extra error in origin time by at least 4 s due to the loss of radio-tracking during the operation (Toksöz et al., 1974). Since ξ=7 explains the travel times for both impacts, we constructed a reference velocity structure based on that ξ parameter.

Text S3. Topography model

For the surface topography model, we employed one of the highest-resolution lunar digital elevation models (DEMs) available today. It is called "SLDEM2015 (Barker et al., 2016)", which was constructed based on the Lunar Orbiter Laser Altimeter (LOLA) data by Lunar Reconnaissance Orbiter (LRO) combined with the DEM produced by Terrain Camera (TC) onboard SELENE (Kaguya). This model covers from ±60 degrees in latitude and ±180 degrees in longitude with the highest horizontal spatial resolution being 59 m. The original data are available on NASA Planetary Data System (PDS).

Concerning the crust-mantle boundary and/or Moho boundary, the crustal structure models (GL0420A) provided by Wieczorek et al. (2013) were utilized. Their models were constructed from the observation of gravity anomalies by the GRAIL mission. Particularly, in order to make it consistent with a density model shown before, we adopted Model 2 which was made with a combination of the GRAIL observation and the crustal thickness (30.8 km at the Apollo 12/14 landing site) estimated from the travel-time analysis using the Apollo seismic data by Lognonné et al. (2003). As the crustal model truncates the degree higher than 310, it provides us the spatial resolution of 0.43 degrees. The original dataset was downloaded from GRAIL Crustal Thickness Archive (Wieczorek et al., 2013).

In addition to the surface and Moho topographies, we also assumed some layers to express the gradual change in the seismic velocity profile with depth. Since the seismic velocity changes rapidly near-surface, we prepared a more densely layered structure at the first 5 km compared to the deeper parts. Following Onodera et al. (2021), the respective boundary depths are defined as:

$$D_i(\theta,\phi) = D_s(\theta,\phi) + \frac{D_M(\theta,\phi) - D_s(\theta,\phi)}{C_i} \quad \text{(S5)}$$

where $D_i(\theta,\phi)$ is the boundary depth of i-th layer at the coordinates of longitude θ and latitude ϕ, and D_s and D_M are the surface elevation from the mean radius of the Moon (1737.4 km) and the Moho

boundary depth, respectively. C_i is a constant to make the mean boundary at the target region (Figure S3) consistent with i-th layer's depth (Table S5). Note that the surface DEM was downsampled to make the spatial resolution match that of Moho boundary model. This kind of procedure makes the deeper structure reflect the Moho undulations and the shallower reflect the surface topographical variations.

Text S4. Parameter study of the correlation length

The simulation results for three correlation-length cases are compared here (a = 0.20, 0.65, 2.0) (Figure S4). In the case of a = 0.20, the envelope looks relatively well fitted with the data, although its spectrogram indicates the surface wave energy is not completely scattered. Compared with the spectrogram of a = 0.65, it is considered that the correlation length of 0.20 km is not large enough to influence the lower frequency components. On the other hand, a = 2.0 shows a strong peak around 140 s in the envelope, which can also be seen as the concentration of energy around 1 Hz in the spectrogram. Therefore, this random medium does not appear suitable for the Apollo 12 landing site.

Text S5. Source assumption

As a source model for impacts, there are two approximations; one is the isotropic radiation with moment tensor and the other is the point force (or body force) expressed with the impulse. In past studies, either model was used to simulate the impact-induced seismic waves (e.g., Blanchette-Guertin et al., 2015; Daubar et al., 2020; Onodera et al., 2021). Since the detailed description of the impacts in terms of source modeling is still an open issue, this study just employed the simplest model, that is, isotropic radiation. In fact, under the intense scattering structure as considered in this study, the source information is lost just after the energy is radiated and the difference in the source model does not so much affect the resultant waveform (i.e., the structure is much more dominant to characterize the seismogram in this case.

In the OpenSWPC, the seismic source M_{src} is given in the form of:

$$M_{src} = M_0 * \dot{f}_{src}(t) * \begin{pmatrix} m_{xx} & m_{xy} & m_{xz} \\ m_{yx} & m_{yy} & m_{yz} \\ m_{zx} & m_{zy} & m_{zz} \end{pmatrix} \quad \text{(S5)}$$

where M_0 is the seismic moment, $\dot{f}_{src}(t)$ is the source time function (the model of Gudkova et al., 2011; 2015 was employed in this study), and m_{ij} $(i, j = x, y, z)$ is moment tensor which defines how seismic energy is released from the source point. Since the moment tensor is normalized form, $\sum {m_{ij}}^2 = 1$. In the case of the isotropic radiation, $m_{ij} = 0$ $(i \neq j)$ and $m_{ij} = 1/\sqrt{3}$ $(i = j)$.

Supporting Figures

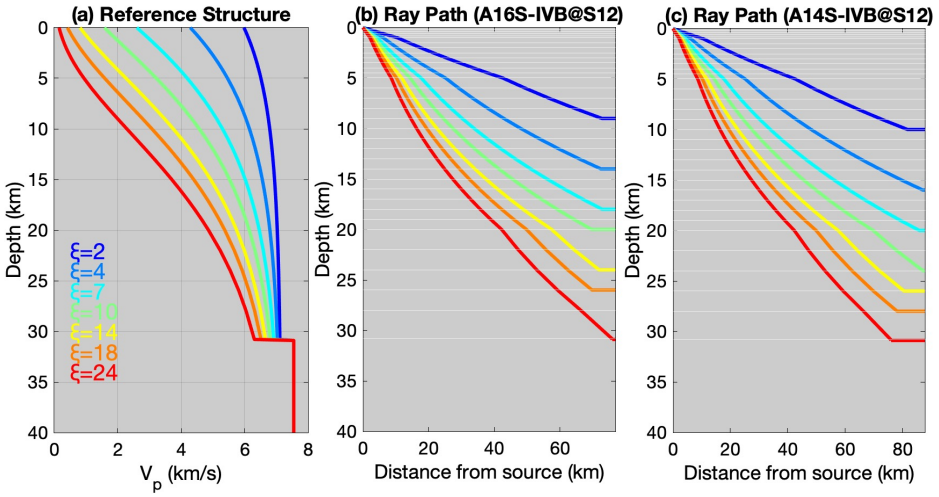

Figure S1. (a) Reference P-wave velocity models based on Equation 4 in Methods (ξ=2, 4, 7, 10, 14, 18, 24). The velocity jump at 30.8 km corresponds to the Moho boundary at the Apollo 12 landing site. P-wave velocity below 30.8 km is from VPREMoon by Garcia et al. (2011). (b) Ray path for each velocity model for Apollo 16 SIVB at Station 12 case. (c) Ray path for each velocity model for Apollo 14 SIVB at Station 12 case. The horizontal axis corresponds to the distance ranging from the source to the halfway through the station.

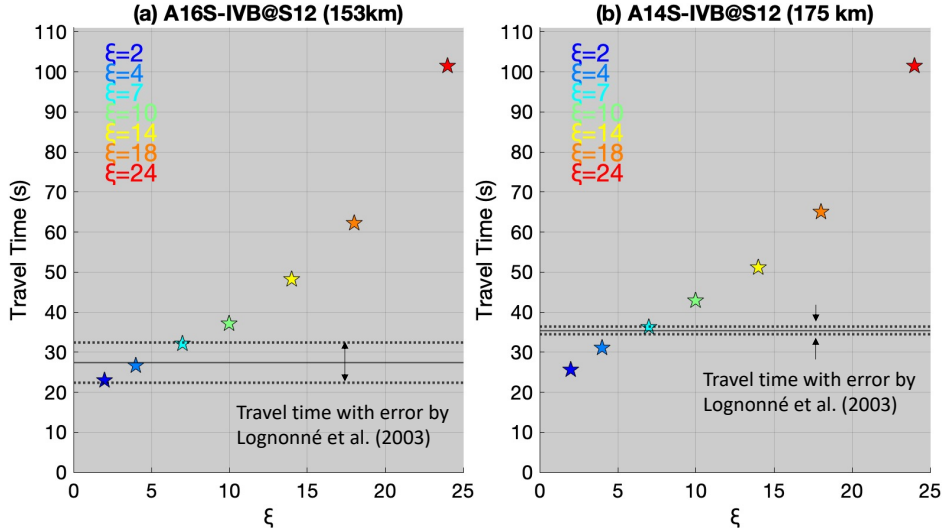

Figure S2. Travel times for respective velocity structure models in Figure S1a for (a) Apollo 16 SIVB at Station 12 case with the epicentral distance of 153.76 km and (b) Apollo 14 SIVB at Station 12 case with the epicentral distance of 175.34 km. The dotted lines show the error range of the travel time determined by Lognonné et al. (2003). The uncertainty of P-wave arrival is 1 s. Note that Apollo 16 SIVB has an additional 4 s error in origin time due to the loss of radio-tracking during its operation (Toksöz et al., 1974).

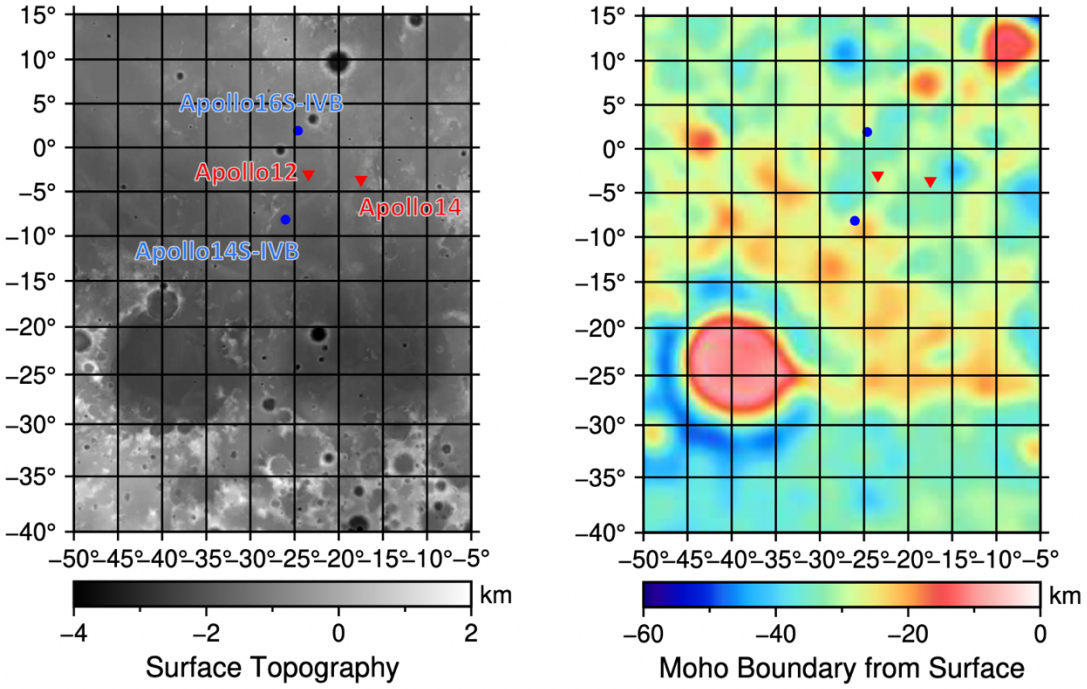

Figure S3. Target region shown as surface topography map (left) and Moho boundary depth (right). Red plots show the locations of the Apollo seismic stations and blue ones show the impacts of Apollo SIVB rocket boosters used in this study.

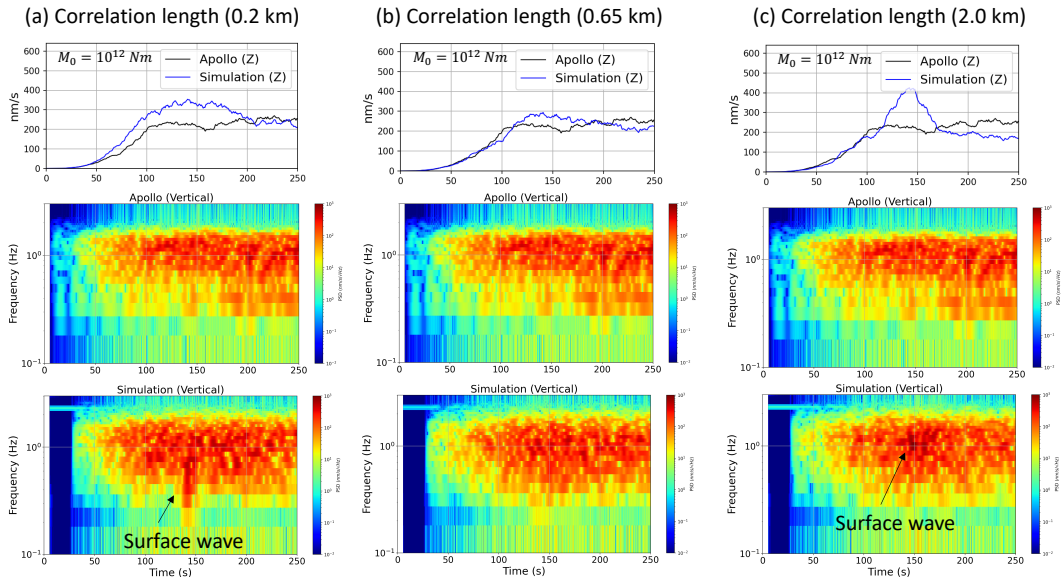

Figure S4. Comparison of synthetics with different correlation length (a: 0.2 km, b: 0.65 km, c: 2.0 km). The top row shows the smoothed envelopes for the vertical component. The black envelopes are for the Apollo data (Apollo 16 SIVB impact), and the blue ones are for the respective simulation cases. The second row displays the spectrogram for the Apollo, and the third row is the spectrogram for the simulation outputs.

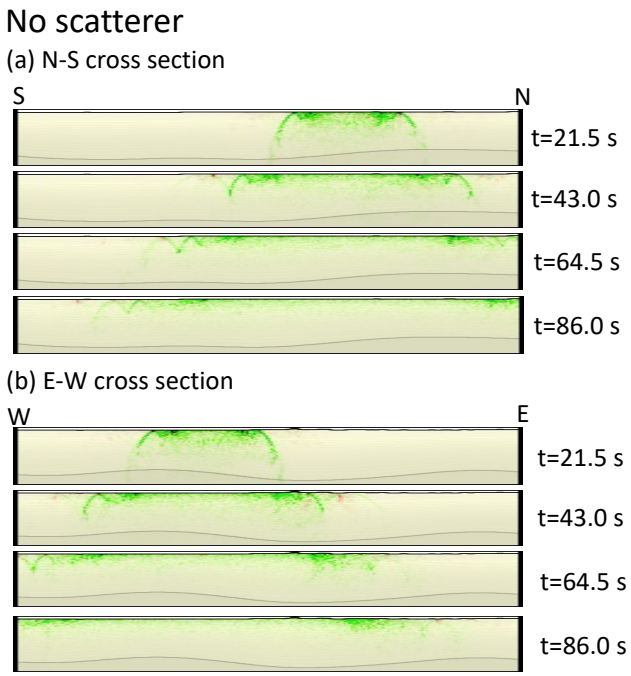

Figure S5. Snapshots of (a) N-S cross section and (b) E-W cross section for the no scatterer case shown in Figure 5 in the main text. Note that the snapshots are decimated by 40 for the horizontal direction and 10 for the vertical direction to reduce the output file size.

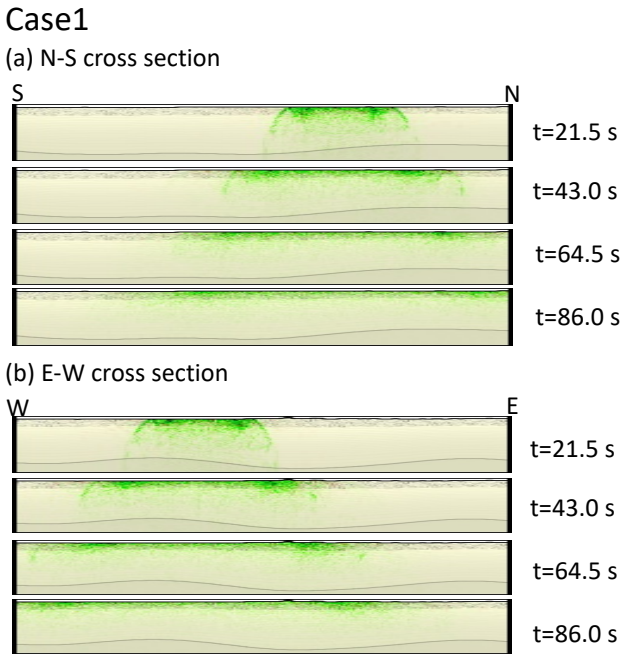

Figure S6. Snapshots of (a) N-S cross section and (b) E-W cross section for Case1 shown in Figure 5 in the main text. Note that the snapshots are decimated by 40 for the horizontal direction and 10 for the vertical direction to reduce the output file size.

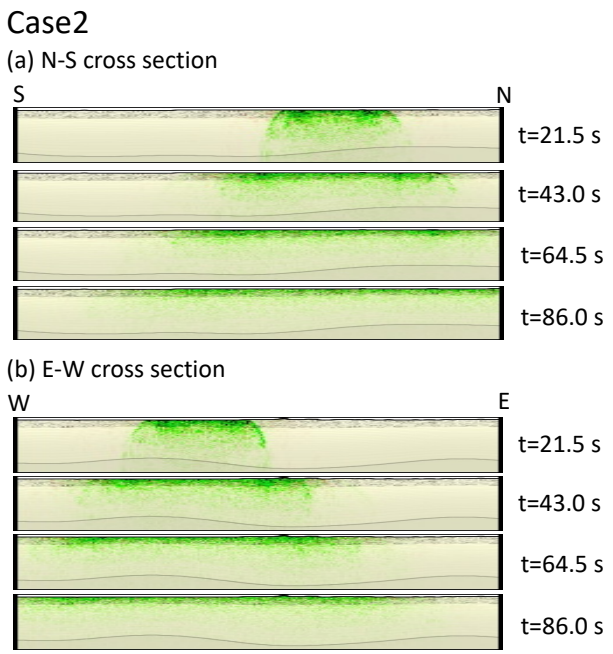

Figure S7. Snapshots of (a) N-S cross section and (b) E-W cross section for Case2 shown in Figure 5 in the main text. Note that the snapshots are decimated by 40 for the horizontal direction and 10 for the vertical direction to reduce the output file size.

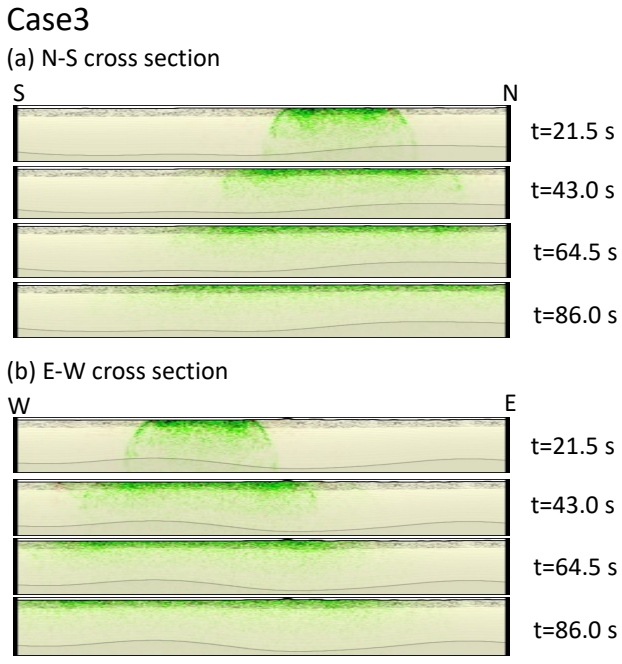

Figure S8. Snapshots of (a) N-S cross section and (b) E-W cross section for Case3 shown in Figure 5 in the main text. Note that the snapshots are decimated by 40 for the horizontal direction and 10 for the vertical direction to reduce the output file size.

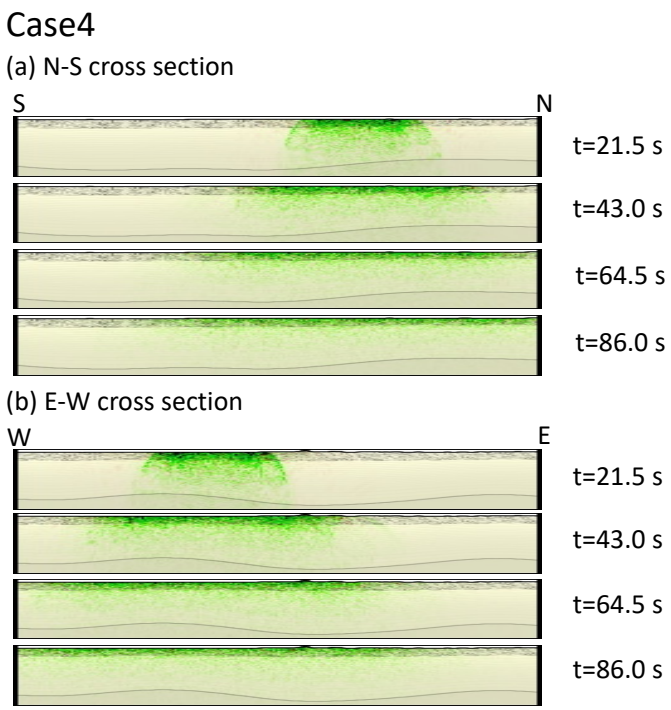

Figure S9. Snapshots of (a) N-S cross section and (b) E-W cross section for Case4 shown in Figure 5 in the main text. Note that the snapshots are decimated by 40 for the horizontal direction and 10 for the vertical direction to reduce the output file size.

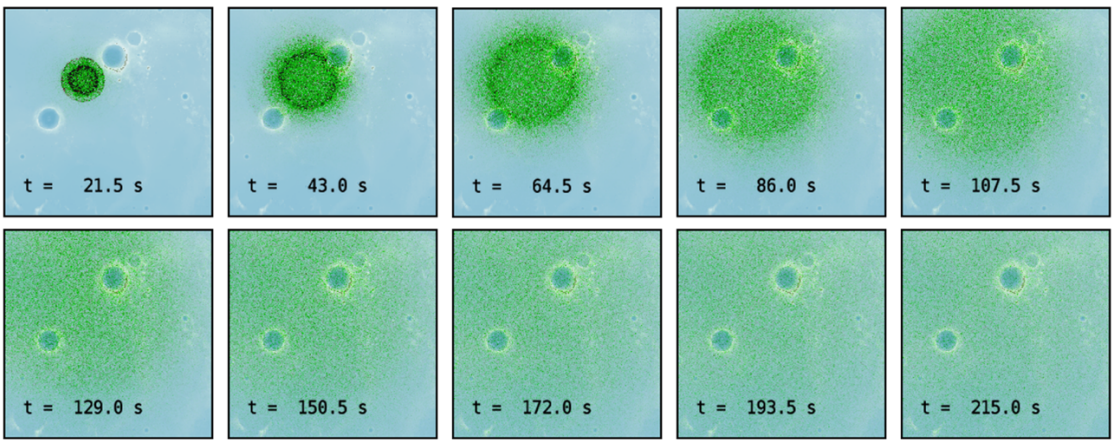

Figure S10. Snapshots for the horizontal plane (Apollo 16 SIVB at Station 12 for Case 4) from 21.5 s to 215.0 s.

Supporting tables

Table S1. Intrinsic Q structure for P- and S-waves assumed in this study.

Layer	$^{P}Q_i$	$^{S}Q_i$	Reference
0 – 10 km	6750	6750	Nakamura and Koyama (1982)
10 – 20 km	5000	5000	Blanchette-Guertin et al. (2012)
20 – 30 km	4000	4000	Blanchette-Guertin et al. (2012)
> 30 km	3750	1500	Nakamura and Koyama (1982)

Table S2. List of general information of Apollo artificial impacts by Toksöz et al. (1974).*These parameters are estimated based on the improved impact location for Apollo16 S-IVB by Wagner et al. (2017).

Impactor	Date	Times received on Earth (UT)	Impact velocity (km/s)	Impact energy (J)
Apollo 12 LM	Nov-20-1969	22h17m17.7s	1.68	3.36×10^{9}
Apollo 14 LM	Feb-7-1971	00h45m25.7s	1.68	3.25×10^{9}
Apollo 15 LM	Aug-3-1971	03h03m37.0s	1.70	3.44×10^{9}
Apollo 17 LM	Dec-15-1972	06h50m20.8s	1.67	3.15×10^{9}
Apollo 13 SIVB	Apr-15-1970	01h09m41.0s	2.58	4.63×10^{10}
Apollo 14 SIVB	Feb-4-1971	07h40m55.4s	2.54	4.52×10^{10}
Apollo 15 SIVB	Jul-29-1971	20h58m42.9s	2.58	4.61×10^{10}
Apollo 16 SIVB	Apr-19-1972	21h02m4s±4s	2.5-2.6*	4.59×10^{10}
Apollo 17 SIVB	Dec-10-1972	20h32m42.3s	2.55	4.71×10^{10}

Table S3. List of impact locations and angles of Apollo artificial impacts. Impact locations of Lunar Modules (LMs) are referred from Toksöz et al. (1974) and those of S-IVB impacts are referred from Wagner et al. (2017). Impact angles and Heading angles are referenced from Orloff (2000).

Impactor	Latitude (°N)	Longitude (°E)	Angle from horizon (°)	Heading angle (N°E)
Apollo 12 LM	-3.94	338.80	3.7	305.85
Apollo 14 LM	-3.42	340.33	3.6	282
Apollo 15 LM	26.36	0.25	3.2	284
Apollo 16 LM	19.96	30.50	-	-
Apollo 13 SIVB	-2.5550	332.1125	76	259.4
Apollo 14 SIVB	-8.1810	333.9695	69	284.3
Apollo 15 SIVB	-1.2897	348.1755	62	276.54
Apollo 16 SIVB	1.9210	335.3770	79	255.3
Apollo 17 SIVB	-4.1681	347.6693	55	277

Table S4. List of parameters. Note that the coordinate system follows that of the OpenSWPC (i.e., $+x$ is north, $+y$ is east, $+z$ points downward). Values in parentheses are for Apollo 16 SIVB impact while values without parentheses are for Apollo 14 SIVB impact.

Parameter name	Symbol	Value
Spatial resolution (km)	d_x	3.5×10^{-2}
	d_y	3.5×10^{-2}
	d_z	3.0×10^{-2}
Time resolution (s)	dt	2.15×10^{-3}
Grid number	N_x	10,500
	N_y	10,500
	N_z	1,350
Time step	N_t	170,000
Corresponding regional space (km)	L_x	367.5
	L_y	367.5
	L_z	40.5
Coordinates at origin (°)	c_{lon}	-26.0305 (-24.623)
	c_{lat}	-8.181 (1.921)
Coordinates at the lower left corner in Cartesian (km)	x_{beg}	-140 (-240)
	y_{beg}	-150 (-140)
Beginning of the vertical plane (km)	z_{beg}	-1.5

Table S5. List of assumed boundaries within the lunar crust. C_i is obtained by dividing the average crustal thickness (28.59 km) at the target region (40°S/15°N/50°W/5°W) with i-th boundary depth.

i-th layer	Mean boundary depth (km)	C_i value	i-th layer	Mean boundary depth (km)	C_i value
1	0.2	142.94	17	9.0	3.176
2	0.4	71.47	18	10	2.859
3	0.6	47.65	19	11	2.599
4	0.8	35.74	20	12	2.382
5	1.0	29.59	21	13	2.199
6	1.5	19.06	22	14	2.042
7	2.0	14.29	23	15	1.906
8	2.5	11.44	24	16	1.787
9	3.0	9.529	25	17	1.682
10	3.5	8.168	26	18	1.588
11	4.0	7.147	27	19	1.505
12	4.5	6.353	28	20	1.429
13	5.0	5.718	29	22	1.299
14	6.0	4.765	30	24	1.191
15	7.0	4.084	31	26	1.100
16	8.0	3.574	32	28	1.021

Table S6. References used in Figure 11a in the main text

Number	Place	Reference
1	Kanto-Tokai, Japan	Fehler et al. (1992)
2	Long Valley, California	Mayeda et al. (1992)
3	Central California	
4	Hawaii	
5	Average in Japan	Hoshiba (1993)
6	Southern California	Jin et al. (1994)
7	Southern California	Leary and Abercrombie (1994)
8	Northern Greece	Hatzidimitriou (1994)
9	Southern Spain	Akinci et al. (1995)
10	Southern California	Adams and Abercrombie (1998)
11	Northeastern Venezuela	Ugalde et al. (1998)
12	Eastern Turkey	Akinci and Eyidogan (2000)
13	Southern Apennines, Italy	Bianco et al. (2002)
14	South Central Alaska	Dutta et al. (2004)
15	Southern Netherlands	Goutbeek et al. (2004)
16	Northeastern Colombia	Vargas et al. (2004)
17	Northeastern Italy	Bianco et al. (2005)
18	Southern Sicily, Italy	Giampiccolo et al. (2006)
19	Asama volcano, Japan	Yamamoto and Sato (2010)
20	Lithosphere and upper mantle	Lee et al. (2003), Lee et al. (2006)
21	Lower mantle (> 670 km depth)	Lee et al. (2003), Lee et al. (2006)
22	Mars	Menina et al. (2021)
23	Mars	Lognonné et al. (2020)
24	Lunar crust	Gillet et al. (2017)
25	Lunar megaregolith	This study

Table S7. References used in Figure 11b in the main text.

Number	Place	Reference
1	Kanto-Tokai, Japan	Fehler et al. (1992)
2	Long Valley, California	Mayeda et al. (1992)
3	Central California	
4	Hawaii	
5	Average in Japan	Hoshiba (1993)
6	Southern California	Jin et al. (1994)
7	Southern California	Leary and Abercrombie (1994)
8	Northern Greece	Hatzidimitriou (1994)
9	Southern Spain	Akinci et al. (1995)
10	Southern California	Adams and Abercrombie (1998)
11	Northeastern Venezuela	Ugalde et al. (1998)
12	Eastern Turkey	Akinci and Eyidogan (2000)
13	Southern Apennines, Italy	Bianco et al. (2002)
14	South Central Alaska	Dutta et al. (2004)
15	Southern Netherlands	Goutbeek et al. (2004)
16	Northeastern Colombia	Vargas et al. (2004)
17	Northeastern Italy	Bianco et al. (2005)
18	Southern Sicily, Italy	Giampiccolo et al. (2006)
19	Asama volcano, Japan	Yamamoto and Sato (2010)
20	Lithosphere and upper mantle	Lee et al. (2003), Lee et al. (2006)
21	Lower mantle (> 670 km depth)	Lee et al. (2003), Lee et al. (2006)
22	Mars	Lognonné et al. (2020)
23	Mars	Menina et al. (2021)
24	Moon	Blanchette-Guertin et al. (2012) Gillet et al. (2017)